Faculty of Physics and Astronomy
University of Heidelberg

Diploma thesis
in Physics

submitted by
Vinzenz Bildstein
born in Bremen
Year 2005

Particle detection at REX-ISOLDE

and

the d(^{30}Mg, ^{31}Mg)p reaction

This diploma thesis has been carried out by Vinzenz Bildstein
at the

Max-Planck-Institut für Kernphysik, Heidelberg

under the supervision of

Prof. Dr. D. Schwalm

Abstract

Due to the production and acceleration method for radioactive ions at REX-ISOLDE, a newly commissioned accelerator, there are three sources for beam contamination: isobaric contamination from the ISOLDE target, isobaric contamination from β-decay while the ions are captured in the REX-trap and charge bred in the EBIS, and stable contamination from the residual gas in the EBIS if the mass to charge ratio allows it to pass the mass separator of REX.

In order to determine the beam contamination qualitatively and quantitatively two 10 μm thick silicon pin-diodes were installed in the beamline behind the target chamber in September 2004. The results of measurements with exotic ^{30}Mg and ^{32}Mg beams are presented in the first part.

In the second part a partial analysis of an experiment employing the (d, p) reaction in inverse kinematics with a ^{30}Mg beam is presented. The aim of this experiment was to study the level scheme of ^{31}Mg and to get additional information about the spin and parity of its states via the angular distribution of the protons emitted.

Zusammenfassung

Aufgrund der Herstellungs- und Beschleunigungsmethode für radioaktive Ionen bei REX-ISOLDE gibt es drei Quellen für eine Strahlverunreinigung: Eine direkte isobare Verunreinigung vom ISOLDE Target, isobare Verunreinigung durch β-Zerfall während des trapping und breedings, sowie stabile Verunreinigung von Restgas aus der EBIS mit dem gleichen A/q.

Um die Strahlverunreinigung qualitativ und quantitativ zu messen, wurden im September 2004 zwei 10 μm dicke Silizium PIN-Dioden im Strahlrohr hinter der Targetkammer installiert. Die Ergebnisse der Messung mit exotischem ^{30}Mg und ^{32}Mg werden im ersten Teil präsentiert.

Im zweiten Teil wird eine teilweise Analyse eines Experiments mit ^{30}Mg-Strahl, das die (d, p) Reaktion in inverser Kinematik verwendet, vorgestellt. Das Ziel dieses Experiments war das Levelschema von ^{31}Mg zu studieren, sowie, wenn möglich, weitere Information zum Spin und Parität der Zustände durch die Protonenwinkelverteilung zu erhalten.

Table of Contents

List of Figures

List of Tables

Chapter 1

Introduction

This thesis consists of two parts. The first part deals with the beam contamination at REX-ISOLDE [1, 2], a user facility for radioactive ion beams (RIBs), which uses the isotope separator on-line (ISOL) method to generate the beam from a mixture of isotopes created by high-energetic protons (1.4 GeV) impinging on a target. The REX-ISOLDE and MINIBALL setup is briefly discussed in section 3.1.

Due to the production and acceleration method for radioactive ions at REX-ISOLDE there are three sources for beam contaminations, which are discussed in section 3.2.

Besides trying to reduce these contaminants it is important to identify the contaminants qualitatively and quantitatively. Knowing the kind and amount of beam contamination is essential in order to extract meaningful results from nuclear experiments. E.g. a recent measurement of the $B(E2;\ 0^+_{\mathrm{gs}} \rightarrow 2^+_1)$-value of ^{30}Mg [3] at REX-ISOLDE was performed by deducing the cross section for beam particle excitation ($\sigma_{\mathrm{CE}}\,(\mathrm{beam})$) relative to the known cross section for target excitation $\sigma_{\mathrm{CE}}\,(\mathrm{target})$ by observing the γ-decay of the inelastically excited states. In this case the cross sections are related by

$$\sigma_{\mathrm{CE}}\,(\mathrm{beam}) = \frac{\varepsilon_\gamma\,(target)}{\varepsilon_\gamma\,(beam)} \cdot \frac{W_\gamma\,(target)}{W_\gamma\,(beam)} \cdot \frac{\mathrm{N}_\gamma(\mathrm{beam})}{\mathrm{N}_\gamma(\mathrm{target})} \cdot \sigma_{\mathrm{CE}}\,(\mathrm{target})$$

where ε_γ is the full peak efficiency of the MINIBALL [4] setup at the energy of the transition and W_γ is the angular correlation of the transition. While the γ-rays from the projectile and the target can be uniquely identified, the source of the target excitation cannot, as target nuclei can also be excited by the beam contaminants, resulting in a wrong cross section if the contamination were not accounted for.

One possibility for ions with charge number $Z \lesssim 20$ is to measure their specific energy loss using a thin silicon detector. In September 2004 two 10 μm thick silicon pin-diodes were installed behind the MINIBALL target chamber in order to determine the beam contamination of neutron rich Mg beams continuously. The results of this measurements and of other methods applied to determine the beam contamination will be presented and compared in chapter 4.

The second part of the thesis contains the analysis of data from an experiment performed at REX-ISOLDE in 2003 to study the single particle structure of ^{31}Mg via the ^{30}Mg(d, p)^{31}Mg transfer reaction in inverse kinematics. Transfer reactions are direct reactions between two nuclei during which one or more nucleons are transferred from one nucleus to the other. In this case a beam of ^{30}Mg was directed on a deuterated polyethylene target to induce the d(^{30}Mg, ^{31}Mg)p reaction in which a neutron is transferred from the deuteron to the magnesium. The transferred nucleon can populate excited states as well as the ground state in the newly formed ^{31}Mg, which - if excited - will decay via emission of one or more γ-rays thus allowing to study the level scheme of ^{31}Mg.

The level scheme of ^{31}Mg is of interest as it lies at the border of the so called "island of inversion" [5]. This region on the nuclear chart is marked by isotopes whose ground state wave functions are dominated by highly deformed intruder states which involve neutron excitations across a melted N = 20 shell gap. A characteristic feature of isotopes belonging to this region are highly collective $E2$ transitions, which were observed in recent experiments [3, 6] for ^{32}Mg but not ^{30}Mg. This shows that while ^{30}Mg is a spherical nucleus outside the "island of inversion", ^{32}Mg is a highly deformed nucleus and thus is fully inside the "island of inversion". This makes the states and spins of ^{31}Mg very interesting as it lies directly on the transition point to the "island of inversion" and provides a sensitive test of shell model calculations.

The setup and the efficiency of this experiment will be discussed in chapter 5 and the methods used in the analysis of the data will be presented in chapter 6. The results of the analysis of the observed γ spectrum and coincident $\gamma - \gamma$ spectra will be shown in chapter 7.

Chapter 2

Underlying Physical Processes

In this chapter the most important physical processes for this work are discussed, which are Rutherford scattering and the energy loss of ions in matter.

2.1 Rutherford Scattering

Rutherford scattering, also know as Coulomb scattering, is due to the Coulomb force between two charged particles. Typically a projectile with charge Z_p, incident with impact parameter b, is deflected by an angle ϑ_{cm} in the Coulomb field of a stationary target particle with charge Z_t. The relationship between b and ϑ_{cm} in the center of mass system can be shown [7] to be

$$\cot\left(\frac{\vartheta_{cm}}{2}\right) = \frac{b}{a_0}, \text{ with } a_0 = \frac{Z_p Z_t e^2}{E_{cm}}, \tag{2.1}$$

where a_0 is half the distance of closest approach in a head-on collision and E_{cm} is the collision energy in the center of mass system (cm).

The differential cross section is the ratio of the number of particles that are incident with an impact parameter between b and $b + \mathrm{d}b$ ($2\pi\ b\ |\mathrm{d}b|$), and the number of particles that are deflected into the solid angle $\mathrm{d}\Omega = 2\pi\ \sin\vartheta_{cm}\ |\mathrm{d}\vartheta_{cm}|$:

$$\frac{\mathrm{d}\sigma}{\mathrm{d}\Omega}(\vartheta_{cm}) = \frac{2\pi\ b\ |\mathrm{d}b|}{2\pi\ \sin\vartheta_{cm}\ |\mathrm{d}\vartheta_{cm}|} = \frac{b}{\sin\vartheta_{cm}}\left|\frac{\mathrm{d}b}{\mathrm{d}\vartheta_{cm}}\right|. \tag{2.2}$$

This leads together with equation (2.1) to the differential Rutherford scattering cross section in the cm-system

$$\frac{\mathrm{d}\sigma}{\mathrm{d}\Omega}(\vartheta_{cm}) = \left(\frac{a_0}{2}\right)^2 \frac{1}{\sin^4\frac{\vartheta_{cm}}{2}}. \tag{2.3}$$

If the energy loss in the target (see section 2.2) is not negligible then the cross section has to be averaged over the target thickness.

In our case only the ratios of the cross sections for the different contaminants are of interest. Since the contaminants have all the same mass and initial laboratory energy E_0 the factors for the transformation between the energy in the laboratory and the cm-system are the same as well as the transformation of the solid angle from the cm-system to the laboratory (as long as relativistic effects can be neglected). Thus the ratio of the cross sections of two types of particles ($Z_{p1},\ Z_{p2}$) with the same mass and initial energy scattered into the same solid angle from the same target is

$$\frac{\sigma_{p1}}{\sigma_{p2}} = \left(\frac{Z_{p1}}{Z_{p2}}\right) \frac{\int_0^d E_2(E_0, x)^{-2} \mathrm{d}x}{\int_0^d E_1(E_0, x)^{-2} \mathrm{d}x}. \tag{2.4}$$

Here $E_n(E_0, x)$ is the laboratory energy of the particle n at the target depth x, i.e. corrected for its specific energy loss in the target.

2.2 Energy Loss of Ions in Matter

The energy loss of ions in matter is caused by interactions of the ion with the electrons as well as with the nuclei of the matter. For the interaction of the ions with the nuclei the Coulomb interaction is predominant, since the cross section for strong interactions is much smaller. Whether interactions with electrons or nuclei dominate the energy loss depends on the kinetic energy of the ion. At high energies the process is dominated by the interaction of the ion with the electrons of the matter as well as complex interactions of the electrons of the ion (if the ion is not completely ionized) with the electrons of the atoms in the matter. These interactions include excitation and ionization of the ions and the target atoms and charge redistribution.

The energy loss $-\mathrm{d}E/\mathrm{d}x$ is the loss of energy E per distance $\mathrm{d}x$. A well know equation for the energy loss of naked ions is the Bethe-Bloch formula:

$$-\frac{\mathrm{d}E}{\mathrm{d}x} = 2\pi N_a r_e^2 m_e c^2 \rho \frac{Z_t}{A} \frac{Z_p^2}{\beta^2} \left[\ln\left(\frac{2m_e\gamma^2 v^2 W_{max}}{I^2}\right) - 2\beta^2 - \delta - 2\frac{C}{Z_t}\right] \tag{2.5}$$

with

I:	mean excitation potential	$\beta =$	v/c of particle
Z_t:	atomic number of target	$\gamma =$	$1/\sqrt{1-\beta^2}$
A:	atomic weight of target	δ:	density correction
ρ:	density of target	C:	shell correction
Z_p:	charge of projectile in units of e	W_{max}:	maximum energy transfer per collision

Aside from the density and shell correction there are other corrections to the Bethe-Bloch formula that increase its validity and accuracy.

There are a few important scaling laws:

- for particles in the same target holds

$$-\frac{dE}{dx} = Z_p^2 f(\beta) \tag{2.6}$$

  i.e. the energy loss depends only on the charge of the projectiles and their velocities.

- Another way to express $\mathrm{d}E/\mathrm{d}x$ is

$$-\frac{dE}{d\varepsilon} = -\frac{1}{\rho}\frac{dE}{dx} = Z_p^2 \frac{Z_t}{A} f(\beta, I), \tag{2.7}$$

  where $d\varepsilon = \rho dx$ is. This means that for targets with not too different Z_t, the energy loss per mass layer ($\mathrm{mg/cm^2}$) is the same.

The equation 2.5 gives accurate results for elementary particles and nuclei up to the α-particle with velocities ranging down to $\beta \gtrsim 0.1$, but for ions relevant in REX-ISOLDE experiments ($\beta \sim 0.05$) the Bethe-Bloch formula has to be modified to account for the partial ionization of the ion.

The calculations of this work were done with the IRMA code [9] which uses the Bethe-Bloch formula (with corrections) to calculate the electronic energy loss of protons in the target and then uses an effective charge Z^* to convert the results for the given particle by multiplying the electronic energy loss of the protons with the square of the effective charge Z^* [10] given by

$$Z^* = Z_p \cdot \left(1 - \frac{1.034 - \frac{0.1777}{e^{0.08114 Z_p}}}{e^{B + 0.0378 \sin(\pi/2\ B)}}\right), \tag{2.8}$$

with

$$B = 0.1772 \frac{\sqrt{E/\mathrm{keV} \cdot A}}{Z_p^{2/3}},$$

where Z_p is the atomic number of the ion, E its energy in keV and A its mass number. The five parameters of the above formula were determined

by fitting the formula to a wide selection of ions and targets [10]. The formula is considered to have an accuracy of about 5 % for ions ranging from carbon to uranium, targets ranging from beryllium to gold and energies above 200 keV/u.

The nuclear stopping power is calculated in IRMA with a formula similar to the one given in [11]

$$\frac{\mathrm{d}E}{\mathrm{d}x}_n = \frac{0.60225}{A} \cdot 8.462 \cdot \frac{Z_p\ Z_t\ M_1}{M\ Z} \cdot \begin{cases} \frac{\ln(1+1.1383\varepsilon)}{2(\varepsilon+0.01321\varepsilon^{0.21226}+0.19593\sqrt{\varepsilon})} & \text{for } \varepsilon \leq 30 \\ \frac{\ln(\varepsilon)}{2\varepsilon} & \text{for } \varepsilon > 30 \end{cases} \tag{2.9}$$

with

$$M = M_1 + M_2 \text{ and } Z = Z_p^{0.23} + Z_t^{0.23}.$$

The total stopping power of a material is the sum of the electronic stopping power (equations 2.5 and 2.8) and the nuclear stopping power (equation 2.9).

The statistical aspect of the scattering of the ions gives additionally rise to an energy straggling that widens the energy spread of a beam after the passage through matter.

Chapter 3

Experimental Setup and Detector Response

In this chapter the experimental setup of REX-ISOLDE and MINIBALL will be shortly explained in section 3.1 and the sources of beam contamination will be discussed in section 3.2. In section 3.3 the calibration of the ΔE detectors and their response in the beam will be discussed as well as some exemplary spectra and the fitting of these spectra.

3.1 Overall Setup

The radioactive ion beams at REX-ISOLDE are generated by bunches of 1.4 GeV protons impinging on a suitable target. The protons are provided by the PS-booster every 1.2 s (if all protons are send to ISOLDE). In a violent reaction of the protons with the target material many different isotopes are produced, which diffuse out of the target, where they are ionized either via surface ionization, in a plasma ion source or in the resonance ionization laser ion source (RILIS). The RILIS makes it possible to selectively ionize elements which are not surface ionized like the alkaline earth metals. The ions that are extracted with an energy of 60 keV from the ISOLDE target are sent through a mass separator, trapped and cooled in the REX trap, charge bred in the EBIS and then accelerated in the REX linear accelerator (see fig. 3.1 and 3.2) to energies between $0.8 - 3.0$MeV/u. The energy spread of the resulting beam is about 1.5 % [2] and the beam spot size is about 5 mm [12].

The resulting beam of radioactive ions is directed onto the target inside the MINIBALL target chamber (see figure 3.3). Inside the target chamber is a double sided stripped silicon detector (called CD detector) [13] located, which is capable of measuring besides the energy (or the energy loss) of the

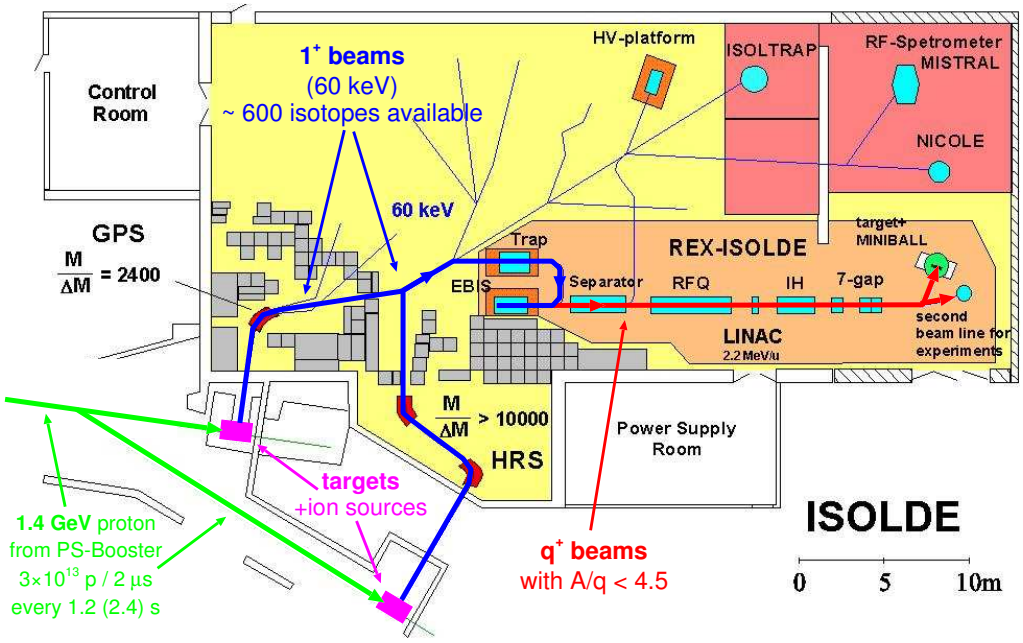

Figure 3.1: Overview of the ISOLDE experimental hall.

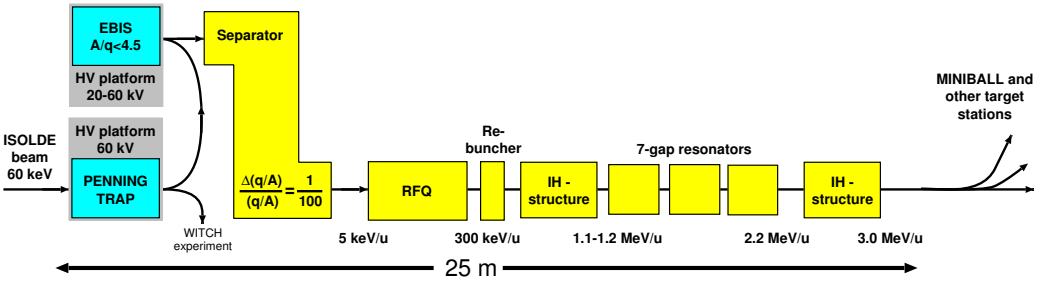

Figure 3.2: Schematics of the REX linear accelerator at ISOLDE.

incident particle its ϑ_{lab} and ϕ angle. This detector consists of 4 segments which each have 16 annular strips at the front and 24 radial strips on the back and the detector located about 30.5 mm behind the target. The inner active radius is 9 mm and the outer active radius is 40.9 mm, which means that the covered laboratory angles are about 15° to 55°. Behind the CD detector a CDE detector consisting of four silicon pads is installed to measure the remaining energy of the particle if passing through the CD detector. Outside the target chamber are the 8 MINIBALL clusters, each consisting of 3 six-fold segmented high purity germanium (HPGe) detectors, which detect the emitted γ-rays with a granularity of about 1cm, if one uses the pulse shape analysis (PSA). Behind the target chamber the two 10 μm thick ΔE silicon

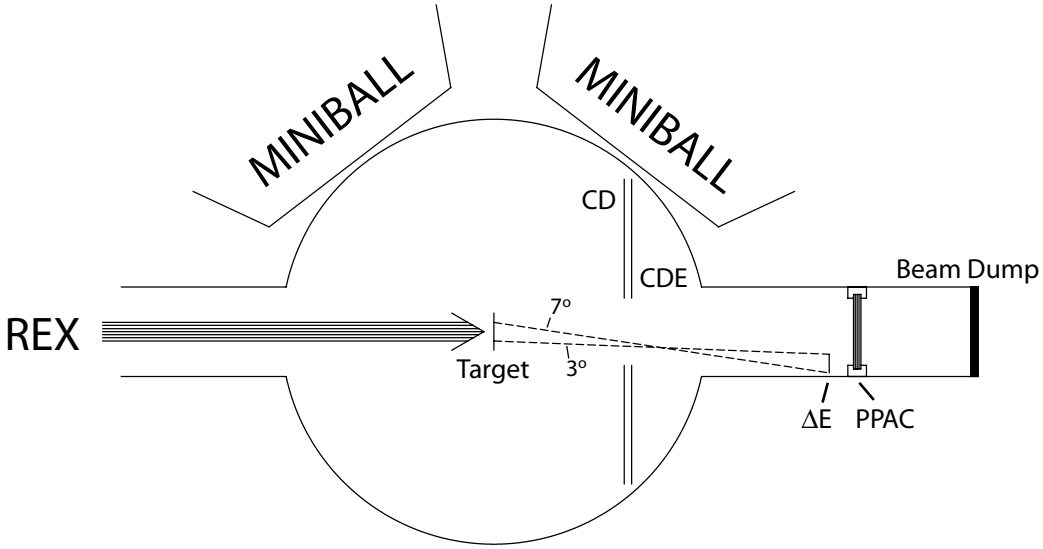

Figure 3.3: Schematic overview of the MINIBALL target chamber including the angles covered by the ΔE silicon detector.

detectors and the PPAC are mounted in front of the beam dump (see figure 3.3).

The resolution of MINIBALL is $< 1\%$ (e.g. 1.03 keV @ 170.5 keV or 6.2 keV @ 1214.7 keV) using the PSA, which increases the position resolution of the γ-rays and thus allows for a better Doppler correction. The width of the peaks is larger than the best a HPGE detector allows because the Doppler correction is not precise enough due to the beam spot size which is about 5 mm. Since the CD detector is at a distance of only 30.5 mm the beam spot size has a big influence on the accuracy of the calculated scattering angle of the detected particles.

3.2 Sources of Beam Contamination

The production method used at REX-ISOLDE to produce radioactive ion beams allows for three sources of beam contamination

(i) Direct isobaric contamination from the ISOLDE target as the general purpose mass separator of ISOLDE is not able to separate all isobars (e.g. ^{30}Mg and ^{30}Al).

(ii) When the ions are captured in the REX-trap and charge bred in the EBIS, part of them may β-decay resulting in an isobaric contamination

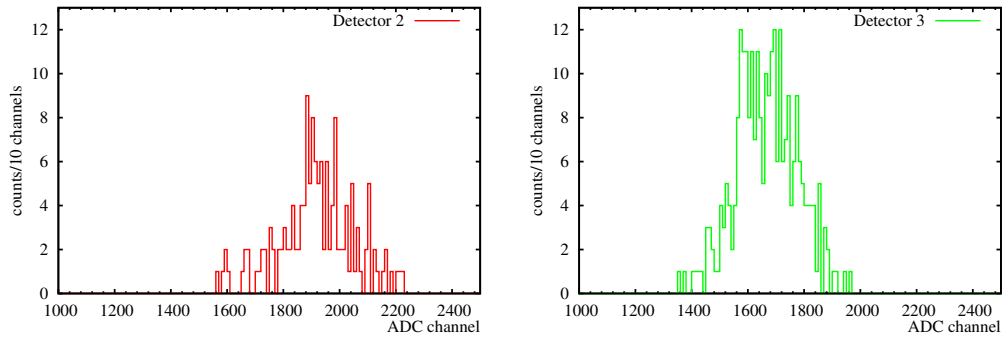

Figure 3.4: Measurement with triple α source at target position.

of the beam (e.g. during 30 ms of trapping and breeding of ^{30}Mg $\approx 6.0\%$ of it will decay to ^{30}Al).

(iii) The beam may contain stable contaminants from the residual gas in the EBIS if their mass to charge ratio allows them to pass the mass separator of REX, which has a resolution of $\frac{\Delta(A/q)}{(A/q)} < 1/100$ [2] (e.g. $^{30}Mg^{8+}$ and $^{15}N^{4+}$ or $^{32}Mg^{9+}$ and $^{32}S^{9+}$).

3.3 ΔE-Detector

In order to continuously measure the beam contamination by small angle scattering after the target two 10 μm thick silicon detectors were mounted directly in front of the PPAC ($\approx$ 15 cm behind the target), at an angle of about 5°. The size of the detectors (1 cm^2) and the beam spot size of about 5 mm resulted in a coverage of scattering angles between 3° and 7° by the detector (see also figure 3.3). The signals of the preamplifier were included in the standard MINIBALL data acquisition system. The detectors were named '2' and '3' corresponding to the electronics channels used. Detector 2 was positioned below the beam while the other detector 3 was to the left of the beam looking in beam direction. The count rates with beam showed that detector 3 was positioned slightly further away from the beam axis than detector 2.

3.3.1 Calibration

In order to calibrate the detectors a triple α source was mounted at the target position. The acquired spectrum (see figure 3.4) shows one peak as expected

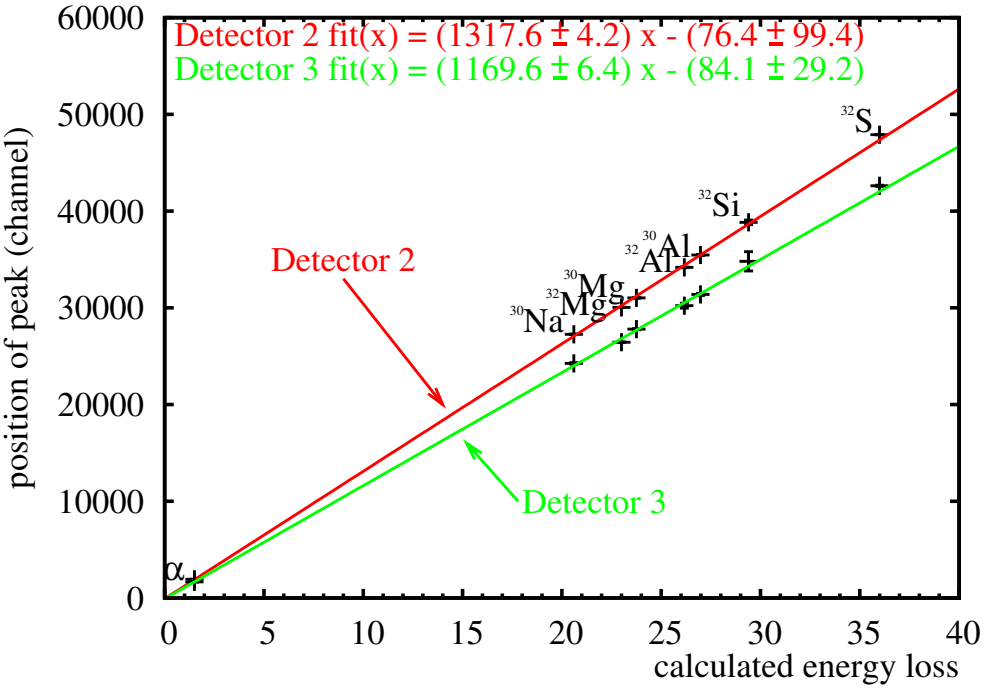

Figure 3.5: Fitted peak position in ADC channels vs. calculated energy loss in the ΔE detector in MeV. The two lines are the fitted gains of the two ΔE detectors (detector 2 is the upper fit) with the parameters shown in the top left corner.

as the resolution of the detectors is not sufficient to resolve the energy loss peaks of the three different α lines.

In order to obtain more calibration points runs with beam were used. In total 8 data points could be used for the calibration of each detector.

Figure 3.5 shows the position of the fitted peaks (in ADC channels) versus the calculated energy loss in the ΔE detectors (in MeV). The data points are measurements with the 1.1 mg/cm^2 ^{107}Ag target and the α source. The lines correspond to linear fits to these data points. The upper (red) line is for detector 2 and the lower (green) line for detector 3. As one can see the values for the thin silver target have a linear dependence and the values of these fits were used as calibration:

$$\begin{aligned} \text{Detector 2}: \quad \text{Energy in MeV} &= 7.590(24) * 10^{-4}\text{ADC} + 0.058(75) \\ \text{Detector 3}: \quad \text{Energy in MeV} &= 8.550(47) * 10^{-4}\text{ADC} + 0.072(25), \end{aligned}$$

where ADC denotes the channel number.

The values for the thicker silver target (4.4 mg/cm^2) do not show a linear dependence, especially for ^{32}S projectiles. The same holds for the values of the ^{30}Mg beam on the thick silver target or the nickel target (3.85 mg/cm^2). As the previously introduced energy loss code IRMA (section 2.2) should have an accuracy of about 5 % for energies above 200 keV/u [10], the large discrepancy can not be explained with the precision of the program (the calculated energy of the ^{32}S after the thick silver target and the detector is about 9 MeV corresponding to 300 keV/u).

Changing the thickness of the detector in a range of ± 10 % did not decrease the reduced χ^2 of the linear fit to all data points significantly, but changing the energy of the incoming beam did show an effect on the reduced χ^2. Figure 3.6 shows the reduced χ^2 for different beam energies. The energies at which the reduced χ^2 is minimal differ somewhat for the two detectors but both seem to indicate that the real beam energy was $5 - 10$ % smaller that the nominal energy, which was 2.865 MeV/u for the ^{30}Mg run and 2.8375 MeV/u for the ^{32}Mg run. These results can of course also be influenced by a slightly thicker target.

As this is a rather large difference and since the results of the two detectors are not conclusive, it will be necessary to confirm this results by remeasuring the beam energy of REX. Therefore the calibration corresponds to the one based on the nominal beam energy and the energy loss values from the thin silver target as shown in figure 3.5 and equation 3.1. Please note that this does not affect the results presented subsequently.

3.3.2 Detector Response with Beam

			energy loss	
target	*projectile*	*detector 2*	*detector 3*	*calculated*
^{107}Ag 1.1 mg/cm^2	^{30}Na	20.74(11)		20.63
^{107}Ag 1.1 mg/cm^2	^{30}Mg	23.62(11)	23.73(13)	23.79
^{107}Ag 1.1 mg/cm^2	^{30}Al	27.00(11)	27.16(15)	27.02
^{107}Ag 4.4 mg/cm^2	^{30}Mg	25.55(11)	25.87(11)	26.51
^{107}Ag 4.4 mg/cm^2	^{30}Al	27.97(12)	28.53(12)	29.95
^{60}Ni 3.85 mg/cm^2	^{30}Na	23.76(11)		23.14
^{60}Ni 3.85 mg/cm^2	^{30}Mg	25.70(11)	26.02(14)	26.72
^{60}Ni 3.85 mg/cm^2	^{30}Al	27.75(12)	28.39(16)	30.10

Table 3.1: Measured and calculated energy loss of ^{30}Mg beam.

Table 3.1 shows the measured energy loss of the different ions of the ^{30}Mg beam in the ΔE detectors in comparison to the calculated values. In order

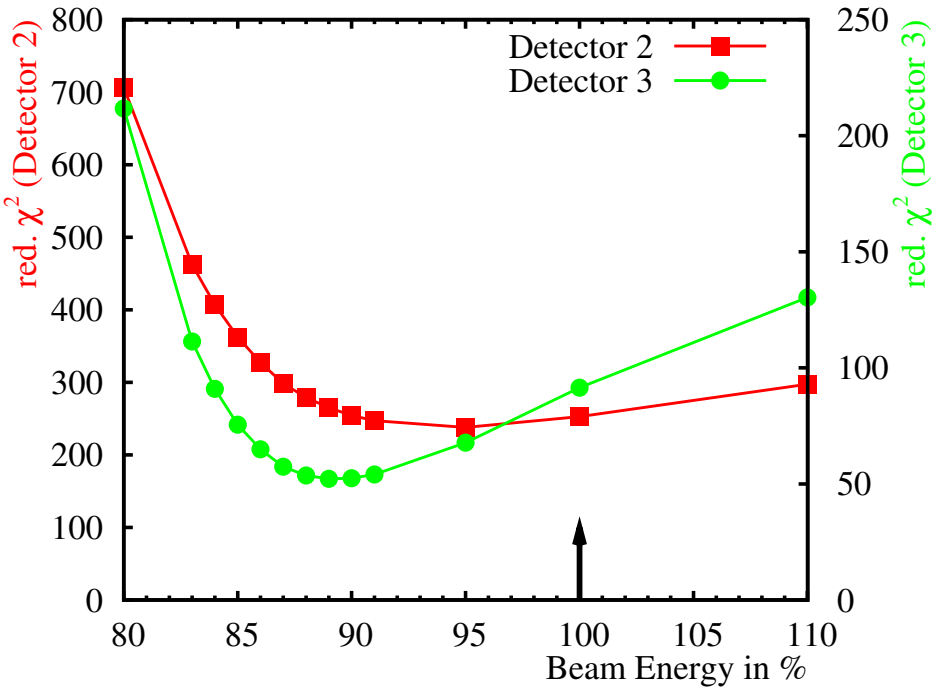

Figure 3.6: Reduced χ^2 of a linear fit to all data points (measured vs. calculated energy loss) versus the beam energy (in % of the nominal beam energy) used in the calculation of the energy loss in the ΔE detectors after the 1.1 mg/cm^2 ^{107}Ag target.

to calculate the values the energy loss was once calculated assuming that the particle undergoes a Rutherford scattering at the beginning of the target and travels then through the target, and once that it first travels through the target and is then Rutherford scattered. The spread in the energy loss comes from multiple factors, namely from

(i) the initial beam energy spread (due to REX),

(ii) different energy losses in the target due to (i),

(iii) (ii) has a spread itself due to energy straggling in the target,

(iv) the beam spot size and the width of the detectors allow for different scattering angles to be detected in the detector ($\approx 3° - 7°$, see figure 3.3) and

(v) all these factors contribute to an energy spread of the scattered particles which in turn creates an greater spread in the energy loss in the detector with additional energy straggling in the detector similar to (ii) and (iii).

These effects add about to an energy spread of $\approx 0.4 - 0.7$ MeV, but the measured peak width ($1 - 2$ MeV) is dominated by the resolution of the ΔE detectors. The measured values given in the table are the results from fits of the data, but the error is mainly due to the error in the calibration of the detectors (see p. 21).

The values for ^{30}Na are missing for detector 3 because the energy resolution of this detector was not good enough to separate the small peak of ^{30}Na in the big tail of ^{30}Mg (see figure 3.11). Also, there are no values for ^{30}Na for the thick silver target for detector 2, because the tail of the ^{30}Mg peak is much stronger than for the nickel target (see figure 3.10). For the thin silver target the measured and calculated values agree very good (they were used for the calibration after all), but for the thicker targets the calculated energy loss is higher than the measured one, except for the ^{30}Na on the ^{60}Ni target. This was discussed already in subsection 3.3.1.

		energy loss		
target	*projectile*	*detector 2*	*detector 3*	*calculated*
^{107}Ag 1.1 mg/cm^2	^{32}Mg	22.86(10)	22.74(13)	23.06
^{107}Ag 1.1 mg/cm^2	^{32}Al	26.00(12)	25.92(24)	26.23
^{107}Ag 1.1 mg/cm^2	^{32}Si	29.48(16)	29.85(31)	29.47
^{107}Ag 1.1 mg/cm^2	^{32}S	36.43(15)	36.43(26)	36.06
^{107}Ag 4.4 mg/cm^2	^{32}Mg	25.09(11)	25.37(14)	25.55
^{107}Ag 4.4 mg/cm^2	^{32}Al	28.28(12)	28.72(16)	29.14
^{107}Ag 4.4 mg/cm^2	^{32}Si	30.63(12)		32.59
^{107}Ag 4.4 mg/cm^2	^{32}S	32.74(13)	33.39(18)	38.27

Table 3.2: Measured and calculated energy loss of ^{32}Mg beam.

Similar to table 3.1 table 3.2 shows the measured energy loss of the different ions of the ^{32}Mg beam in the ΔE detectors in comparison to the calculated values.

The values for the thin silver target are in good agreement with the calculated values, but the values for the thick silver target differ somewhat (see also the discussion in subsection 3.3.1).

Especially do the calculated values not show a lower energy (loss) for ^{32}S in the detectors for the thicker target. However the assignment of ^{32}S to the top peak of figure 3.8 is unambiguous as ^{32}S is the only stable isotope (intensity doesn't depend on the time since the last proton pulse) with the right A/q for which the calculated values come even close to the measured ones.

There is no value for the ^{32}Si for detector 3, because the resolution of

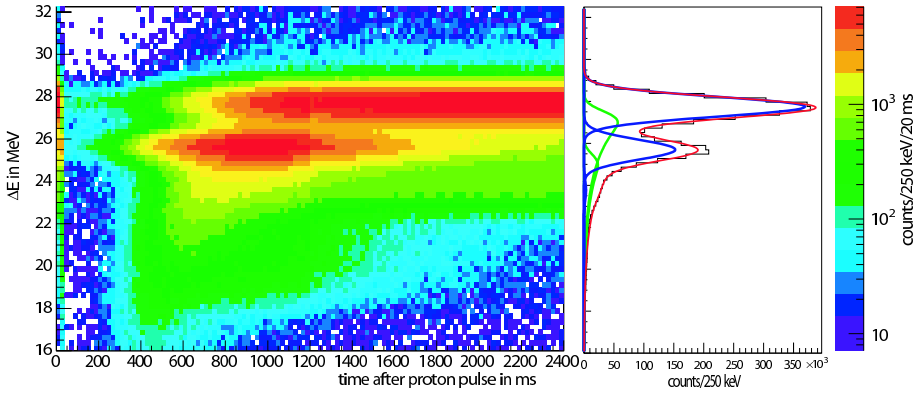

Figure 3.7: Beam of ^{30}Mg on the ^{60}Ni target, results of detector 2 after 48 hours of beam time. The energy loss versus the time after the proton pulse is shown two dimensional in the left panel (^{30}Al at 28 MeV and ^{30}Mg at 26 MeV) and the projection onto the energy loss axis in the right panel.

this detector is not good enough to distinguish the small ^{32}Si peak from the much bigger ^{32}S peak.

3.3.3 Spectra and Fitting

Figure 3.7 shows the energy loss in detector 2 versus the time after the protons impact on the ISOLDE target (left panel). ^{30}Mg has an energy loss of $\approx$ 26 MeV and ^{30}Al an energy loss of $\approx$ 28 MeV. The right panel shows the projection of the left panel onto the energy loss axis.

One can clearly see that there is a breakdown of the count rate directly after the proton pulse for about 300 ms. This is caused by the high instantaneous rate at the detector which is due to the thick target (higher energy loss means greater cross section for Rutherford scattering) and the time structure of the REX-ISOLDE beams, as the instantaneous rate is about 4 orders of magnitude higher than the average rate. Since most of the magnesium comes in the first 600 ms while the aluminum intensity is almost constant, this breakdown distorts the measured ratio between the two components in the beam. As mentioned in section 3.1 is detector 3 at a slightly larger angle, so that the breakdown is not as long nor as strong as for detector 2, but it is still too strong to get useful results for the beam contamination.

In order to determine the amount of beam contamination the following fit function was used for fitting the energy loss spectra. The form of the peaks is a gauss peak (A) plus a tail (B), except for the measurements with ^{32}Mg on the thin silver target as well as the ^{32}Si and ^{32}S peaks which were

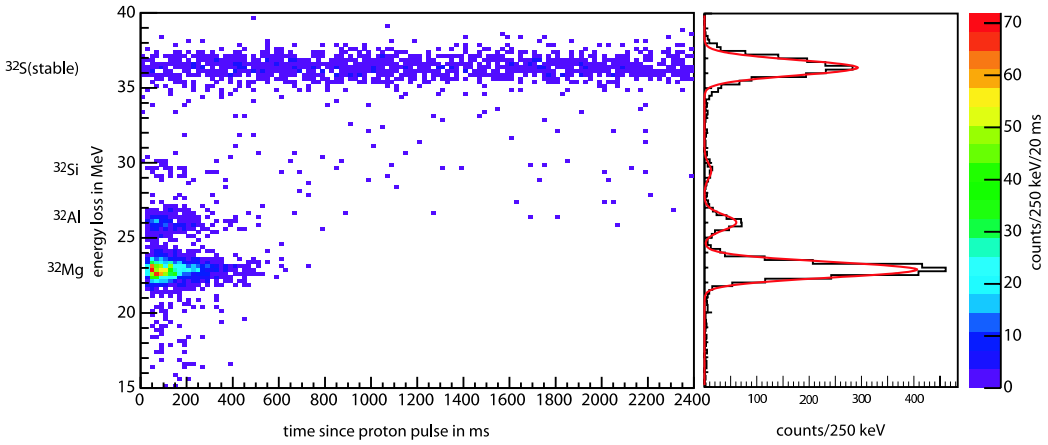

Figure 3.8: Beam of ^{32}Mg on the thin ^{107}Ag target, results of detector 2 after $\approx$ 1 hour of beam time.

fitted without a tail

$$A(x) = \frac{a}{\sigma\sqrt{2\pi}}\, exp\left(-\frac{(x-x_0)^2}{2\sigma^2}\right) \tag{3.1}$$

$$B(x) = t_p\ a\ \exp(\lambda\ (x-\overline{x_0}))\ \mathrm{erfc}\left(\frac{x-\overline{x_0}}{\sigma}\right) \tag{3.2}$$

$$\overline{x_0} = x_0 - \eta\ 2\ \sqrt{2\ \ln(2)}\ \sigma$$

with a as area of the gauss peak, x_0 its mean and σ its resolution. The parameter η determines the position of the tail in units of σ. t_p is the height of the tail relative to the area of the gauss peak and λ determines how steep the tail falls off.

To fit the ^{30}Mg runs on the ^{60}Ni and the thin silver target three peaks without background were used for detector 2, while the fit function for detector 3 consists only of two peaks, since the little bump in the tail of the lower peak (^{30}Mg) which is the ^{30}Na is not visible in the spectrum of this detector. The peaks have all the same resolution (σ).

As mentioned before are the combined tails of ^{30}Mg and ^{30}Al too big to fit the ^{30}Na peak for the thick silver target, so only two peaks were used to fit the results of these runs for both detectors.

Figure 3.8 shows on the left the energy loss versus the time after the proton pulse impacted on the ISOLDE target and on the right a projection of the same plot. As one can see there is another source of contamination present which was not observed for the ^{30}Mg case, namely a weak stable ^{32}S component from the residual gas of the EBIS. There are three radioactive components of the beam besides ^{32}Mg ($t_{1/2} = 95(16)$ ms), ^{32}Al ($t_{1/2} = 33(4)$

ms) and ^{32}Si ($t_{1/2}$ = 132(13) a) can be seen. The short lifetime of ^{32}Al suggests that the observed ^{32}Al stems mostly from β-decay of ^{32}Mg since a contribution from the ISOLDE target would only appear in the first time bin of figure 3.8.

Please note that the ^{32}S contamination can be identified in the CD detector due to the very different Z and the resulting very different energy losses in the target. It is therefore not considered subsequently.

As one can see in figure 3.8, there are no counts for ^{32}Mg more than 600 ms after the proton pulse hit the ISOLDE target, and for practical purposes only events less than 400 ms after the proton pulse are considered. This of course reduces the area of the ^{32}S peak in the spectrum on the right side of figure 3.8 by a factor of 6 (2400/400), since the intensity of the stable ^{32}S does not depend on the time after the proton pulse.

The fit function used for fitting the energy loss with the 1.1 mg/cm^2 target is the same for both detectors, four gauss peaks (equation 3.1) of which three (for ^{32}Mg, ^{32}Al and ^{32}Si) have the same resolution (σ). The fit function for the thick silver target is a bit more complex, due to the tail of the peaks.

For detector 2 a function with four gauss peaks (equation 3.1) was chosen of which again the three peaks for ^{32}Mg, ^{32}Al and ^{32}Si have the same resolution and the ^{32}Mg and ^{32}Al peaks also have a tail (equation 3.2).

Because the ^{32}Si peak is very small a tail would be even smaller and would lead to problems during the fitting since the peak lies in the lower flank of the ^{32}S peak. Due to these reasons it was chosen not to fit a tail to this peak, even though it would make sense to treat all the peaks the same.

The fact that the peak of ^{32}S is much broader than the other peaks might be attributed to the fact that the energy loss in the target and the detector is much higher, and since the ^{32}S can be distinguish from the other beam components in the CD detector the fit of this peak is not crucial.

Since the resolution of detector 3 is not good enough to distinguish the ^{32}Si peak from the ^{32}S peak, the fit function for this detector is essentially just the fit function used for detector 2 without the gauss peak for ^{32}Si.

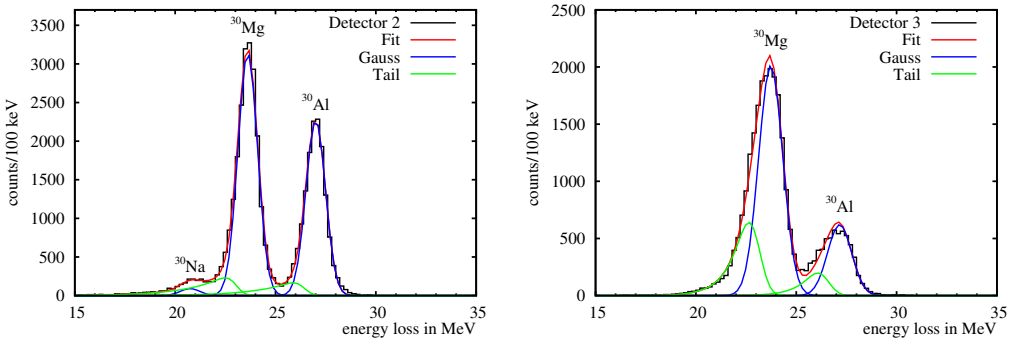

Figure 3.9: Measurement with ^{30}Mg beam on a 1.1 mg/cm^2 ^{107}Ag target, only events less than 1200 ms after proton pulse, with fitted curves.

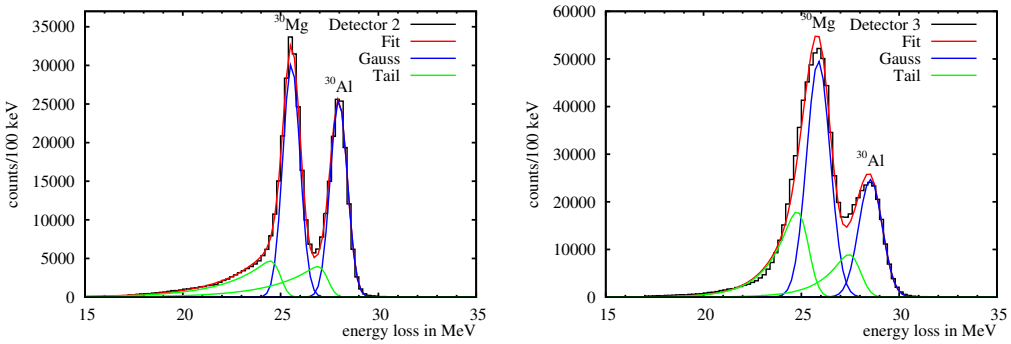

Figure 3.10: Measurement with ^{30}Mg beam on a 4.4 mg/cm^2 ^{107}Ag target, only events less than 1200 ms after proton pulse, with fitted curves.

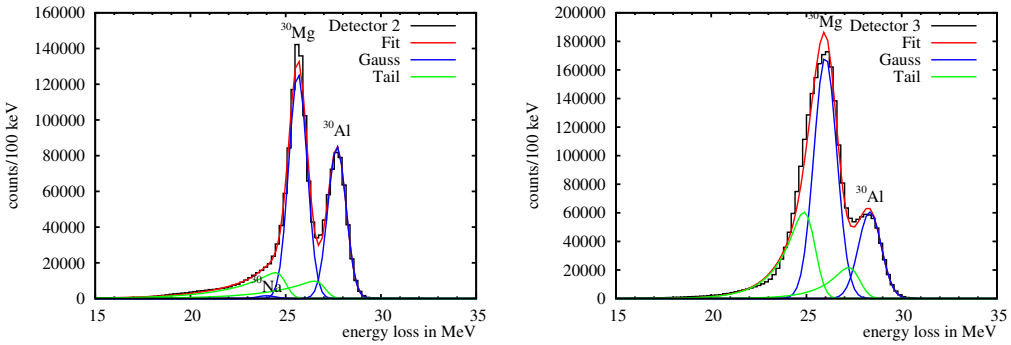

Figure 3.11: Measurement with ^{30}Mg beam on a 3.85 mg/cm^2 ^{60}Ni target, only events less than 1200 ms after proton pulse, with fitted curves. Note the very small peak of ^{30}Na in the left panel at about 24 MeV.

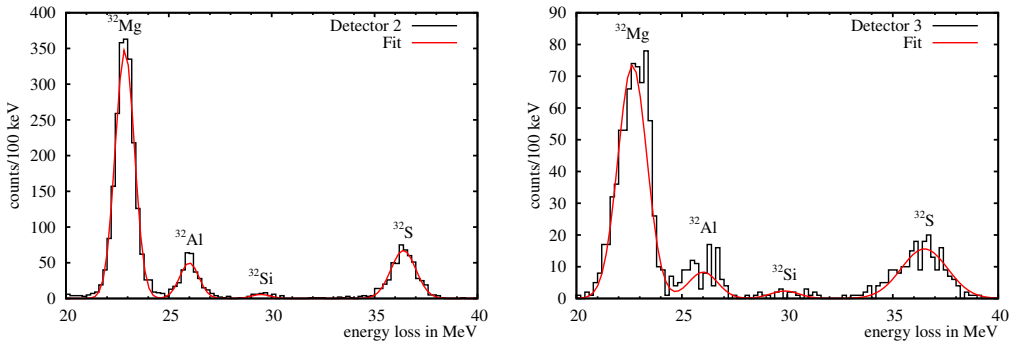

Figure 3.12: Measurement with ^{32}Mg beam on a 1.1 mg/cm^2 ^{107}Ag target, only events less than 400 ms after proton pulse, with fitted curves.

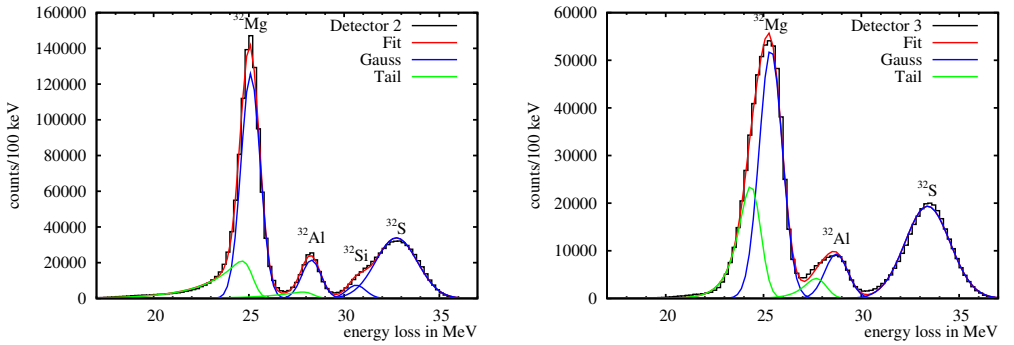

Figure 3.13: Measurement with ^{32}Mg beam on a 4.4 mg/cm^2 ^{107}Ag target, only events less than 400 ms after proton pulse, with fitted curves.

Chapter 4

Results

4.1 ^{30}Mg

4.1.1 ΔE detector

Due to the breakdowns and the resulting distortion of the ratio between magnesium and aluminum (see section 3.3), it is impossible to get a continuous measurement of the contamination using the ΔE detectors. But the one hour measurement with the thin silver target yielded better results for detector 3 which has a lower count rate (see section 3.3) and thus does not have a very strong breakdown in the count rate after proton impact. This measurement allows to establish an upper limit on the beam contamination:

$$\frac{I_{\mathrm{Al}}}{I_{\mathrm{Mg}} + I_{\mathrm{Al}}} = \frac{\alpha N_{\mathrm{Al}}}{N_{\mathrm{Mg}} + \alpha N_{\mathrm{Al}}} < 20.81(26)\%$$

with $\alpha = \frac{\sigma_{\mathrm{Mg}}}{\sigma_{\mathrm{Al}}}$ (see section 2.1) and with the time after the proton pulse limited to 1.2 s.

It was possible to confirm that this upper limit is not too far from the actual beam contamination by using a combination of other methods to measure the contamination, which are discussed in subsection 4.1.2.

4.1.2 Other Methods

Besides the direct measurement with the ΔE detector there are other methods to measure the beam contamination, which exploit different features of the sources of contamination. These methods do not all measure the total contamination, but some of them only measure the contamination directly from the ISOLDE target and not the contribution from β-decay during the trapping and breeding. The used methods were

- the analysis of the release curve (only ISOLDE contribution and residual gas from EBIS with same A/q),
- a RILIS on/off measurements (only ISOLDE contribution and residual gas from EBIS with same A/q),
- the measurement of β-decay lines in the beam dump (total radioactive contamination, not stable residual gas from EBIS with same A/q) and
- the calculation of the β-decay yield, during trapping and breeding.

These four methods will shortly be explained in the following and a comparison of these four methods will be made.

β-decay

The β-decay yield during the trapping and breeding is calculated as follows. The decay law presented is for a radioactive chain of N isotopes where isotope i ($i = 1 \ldots N$) decays to isotope $i+1$. The initial conditions are $n_i(0) = 0$ for $i > 1$ and $n_1(0) = 1$, where $n_i(t)$ is the fractional abundance of isotope i at time t. The rate of change of isotope n_i is then given by

$$\dot{n}_i = \lambda_{i-1} \cdot n_{i-1} - \lambda_i n_i \tag{4.1}$$

where λ_i is the decay constant of isotope i ($\lambda = 1/\tau = \ln 2/t_{1/2}$) and the β_n, β_{2n}, ... branches were neglected. This is a set of linear differential equations. With the given initial conditions the solution for $n_i(t)$ is

$$n_i(t) = \prod_{j=1}^{j=i-1} \lambda_j \cdot n_1(0) \sum_{j=1}^{i} \frac{e^{-\lambda_j t}}{\prod\limits_{\substack{k=1 \\ k \neq j}}^{i} \lambda_k - \lambda_j}, \; i > 2. \tag{4.2}$$

For the case of $N = 3$

$$n_1(t) = e^{-\lambda_1 t} \tag{4.3}$$

$$n_2(t) = \lambda_1 \frac{e^{-\lambda_1 t} - e^{-\lambda_2 t}}{\lambda_2 - \lambda_1} \tag{4.4}$$

$$n_3(t) = \lambda_1 \lambda_2 \left(\frac{e^{-\lambda_1 t}}{(\lambda_2 - \lambda_1)(\lambda_3 - \lambda 1)} + \frac{e^{-\lambda_2 t}}{(\lambda_1 - \lambda_2)(\lambda_3 - \lambda_2)} + \frac{e^{-\lambda_3 t}}{(\lambda_1 - \lambda_3)(\lambda_2 - \lambda_3)} \right) \tag{4.5}$$

As the ions are captured in the trap almost continuously the trapping time is not constant, in contrast to the fixed breeding time in the EBIS. Therefor $n_i(t)$ has to be averaged over the corresponding time span. Integrating equation 4.2 from t_1 (= breeding time) to t_2 (= breeding time plus maximum trapping time) and dividing by $t_2 - t_1$ gives for the first three isotopes

$$\frac{\int_{t_1}^{t_2} n_1(t)\ \mathrm{d}t}{t_2 - t_1} = \frac{100}{\lambda_1}\frac{e^{-\lambda_1 t_1} - e^{-\lambda_1 t_2}}{t_2 - t_1} \tag{4.6}$$

$$\frac{\int_{t_1}^{t_2} n_2(t)\ \mathrm{d}t}{t_2 - t_1} = \frac{100}{\lambda_2(\lambda_1 - \lambda_2)(t_1 - t_2)}\left[\lambda_2\left(e^{-\lambda_1 t_1} - e^{-\lambda_1 t_2}\right) - \lambda_1\left(e^{-\lambda_2 t_1} - e^{-\lambda_2 t_2}\right)\right] \tag{4.7}$$

$$\frac{\int_{t_1}^{t_2} n_3(t)\ \mathrm{d}t}{t_2 - t_1} = \frac{100}{t_2 - t_1}\left[\frac{\lambda_2\left(e^{-\lambda_1 t_1} - e^{-\lambda_1 t_2}\right)}{(\lambda_1 - \lambda_2)(\lambda_1 - \lambda_3)} + \frac{\lambda_1\left(e^{-\lambda_2 t_1} - e^{-\lambda_2 t_2}\right)}{(\lambda_2 - \lambda_1)(\lambda_2 - \lambda_3)} + \frac{\lambda_1\lambda_2\left(e^{-\lambda_3 t_1} - e^{-\lambda_3 t_2}\right)}{\lambda_3(\lambda_3 - \lambda_1)(\lambda_3 - \lambda_2)}\right] \tag{4.8}$$

For the ^{30}Mg beam a breeding time of 16(2) ms was used and the length of one EBIS cycle was 1/49 s. Using equation 4.7 with $t_{1/2}(^{30}\mathrm{Mg}) = 335(17)$ ms and $t_{1/2}(^{30}\mathrm{Al}) = 3.60(16)$ s a beam contamination of 5.26(38)% ^{30}Al from β-decay during the trapping and breeding is expected.

Analysis of the Release Curve

The release curve shows the intensity of the beam in relation to the time after the proton pulse impact on the ISOLDE target. Due to different release time of the various isotopes from the target an analysis of the release curve can be used to extract the beam purity. As the intensity of contamination that stems from the β-decay has the same time dependency as the parent nucleus this contribution is not accounted.

Figure 4.1 shows this relation as the number of detected particles in the CD detector versus the time after the proton pulse. The steps in the intensity are caused by the fact that the proton pulses hit the ISOLDE target at 1.2 or 2.4 s intervals, in rare cases even longer times.

There are two components visible in the spectrum of figure 4.1, one with a fast ($\approx$ 120 ms) and one with a slow ($\approx$ 4 s) decay, attributed to the two

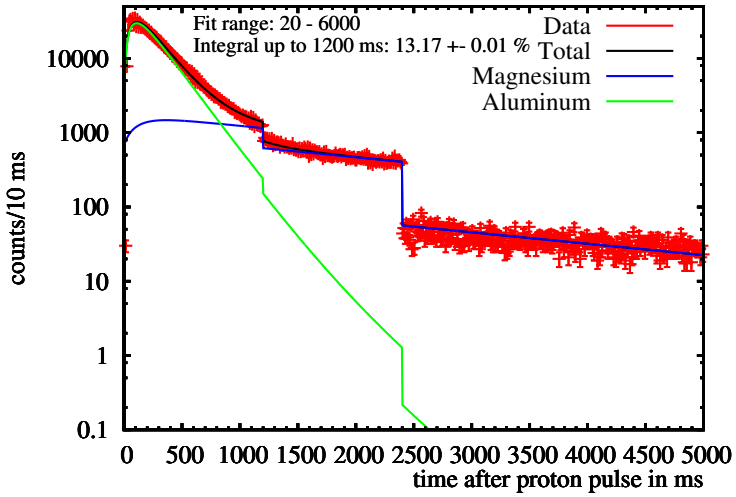

Figure 4.1: Number of events in the CD detector versus time after proton pulse and the release curve.

main beam components ^{30}Mg ($t_{1/2} = 335(17)$ ms) and ^{30}Al ($t_{1/2} = 3600(160)$ ms). Using the formula for the release curve [14]

$$P(t, \lambda_r, \lambda_f, \lambda_s, \alpha) = \frac{1}{\text{Norm}} \left(1 - e^{-\lambda_r t}\right) \left[\alpha e^{-\lambda_f t} + (1 - \alpha)\, e^{-\lambda_s t}\right], \qquad (4.9)$$

where the first term describes the rise after proton impact (λ_r). It was observed that the subsequent decay of the release curve has two components, one fast (λ_f) and one slow (λ_f) component whose ratio is described by α. The measured release curve was fitted with

$$P_{tot} = N_{\text{Mg}} P_{\text{Mg}} + N_{\text{Al}} P_{\text{Al}}, \qquad (4.10)$$

where N_{Mg}, N_{Al}, λ_f^{Mg} and λ_s^{Al} were varied during the fit, while λ_r, λ_s^{Mg} and α were taken from [15].

The determined release time is $(\lambda_f(^{30}\text{Mg}) \cdot \ln 2)^{-1} = 140(2)$ ms, while the half-life of ^{30}Mg (335(17) ms) folded with the release time of stable magnesium (190 ms) [15] gives 121(2) ms, which is a good agreement considering the different conditions during the measurements. The fit gives a beam contamination of 13.17(1)% ^{30}Al in the beam. This methods measures only contamination from ISOLDE and the EBIS since contamination from the β-decay of ^{30}Mg during the trapping and breeding has the same time structure as ^{30}Mg.

RILIS on/off measurement

The RILIS on/off measurement is a simple comparison of counts in the CD detector while the laser ion source RILIS is on or off. This gives a value for the beam contamination from ISOLDE alone as there is no ^{30}Mg in the beam without the RILIS on and thus there is also no β-decay of ^{30}Mg during trapping and breeding. Stable contamination from the residual gas of the EBIS is also measured by this methods, but no stable contamination was observed for a ^{30}Mg beam.

Beam Dump

The measurement of the γ-rays from the β-decay of ^{30}Mg and ^{30}Al with the beam dump detector gives a value of the total radioactive beam contamination from the ISOLDE target as well as from the β-decay during trapping and breeding. Stable contaminants from the EBIS are of course not detected with this method.

Comparison of Methods

Method	*Amount of ^{30}Al in %*	*Contribution from trapping and breeding*	*ISOLDE*
ΔE measurement	$< 20.81(26)$	x	x
β-decay	5.26(38)	x	
release curve	13.17(1)		x
RILIS on/off	12.73(71)		x
beam dump	17.3(27)	x	x
total	18.41(38)	x	x

Table 4.1: Results of different methods to measure the beam contamination up to 1.2 s after the proton pulse for a beam of ^{30}Mg with 2.685 MeV/u on a 3.85 mg/cm^2 ^{60}Ni target.

Table 4.1.2 shows the results from the different methods that were used to determine the beam contamination of the ^{30}Mg beam up to 1.2 s after the proton pulse for a beam of ^{30}Mg with 2.685 MeV/u on a 3.85 mg/cm^2 ^{60}Ni target. The different methods measure different contributions, namely the analysis of the release curve and the RILIS on/off measurement only measure contamination from ISOLDE and stable residual gas from the EBIS and the beam dump method only measures the radioactive contamination.

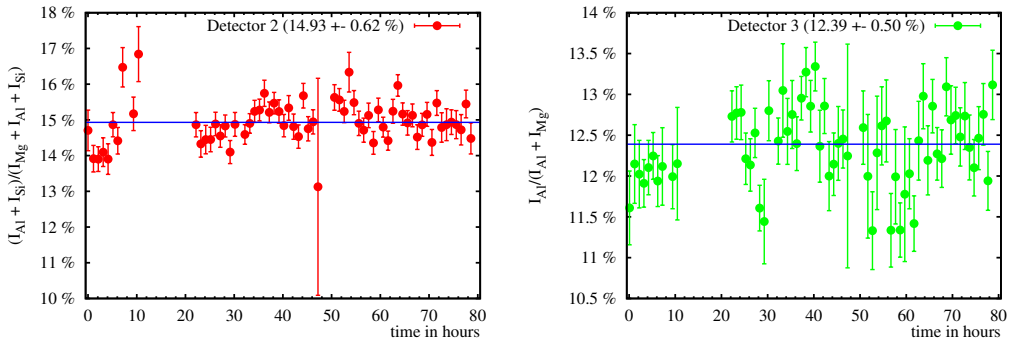

Figure 4.2: Contamination of the beam of ^{32}Mg on the thick ^{107}Ag target. On the left panel the percentage of aluminum and silicon as measured with detector 2 and on the right panel only the percentage of aluminum in the beam measured with detector 2 since the resolution of detector 3 is not sufficient to distinguish the small peak of silicon from the otherwise uninteresting sulfur. The horizontal lines represent the weighted average of all data points. The time after the proton pulse is limited to 400 ms.

Contamination from stable residual gas from the EBIS could be dismissed by measurement without protons. The only remaining contaminations are thus directly from the ISOLDE target or through β-decay during the trapping and breeding. The results of the different methods are in good agreement. The total result of these measurements was obtained by averaging the two values that measure only the beam contamination from ISOLDE (release curve analysis and RILIS on/off measurement), adding the expected β-decay to the results. A weighted average of this result with the result of the beam dump measurement yields the total amount of ^{30}Al in the beam to be 18.41(38) %. This is consistent with the limit given in subsection 4.1.1.

4.2 ^{32}Mg

Here a run of about 3.5 days was analyzed with the same methods as for ^{30}Mg (section 4.1), but the time after the proton pulse was limited to 400 ms instead of 1.2 s. In order to investigate the development of the contamination during these 3.5 days of the fall 2004 running period the events were accumulated for one hour and then fitted, thus giving every hour a value for the beam contamination. There were some times without a beam (due to a failure of REX or the PS-booster), visible as times without a measurement of the beam contamination.

The left plot of figure 4.2 shows the beam contamination of ^{32}Al and ^{32}Si measured with detector 2 over the time of the experiment and the right plot shows only the amount of ^{32}Al in the beam, as it is not possible to separate the ^{32}Si from the ^{32}S with detector 3, due to the poor resolution. The two plots of figure 4.2 show that the beam contamination is mostly independent of time except for small fluctuations which could be due to a variation of the ISOLDE target temperature, caused e.g. by more or less proton pulses provided by the PS-booster.

^{107}Ag target	*contaminant*	*measured*	*from β-decay*
Detector 2			
1.1 mg/cm^2	^{32}Al	10.99(36) %	13.1(21) %
1.1 mg/cm^2	^{32}Si	2.02(25) %	4.26(88) %
4.4 mg/cm^2	^{32}Al	14.93(26) %	17.4(23) %
Detector 3			
4.4 mg/cm^2	^{32}Al[1]	12.39(50) %	13.7(19) %

Table 4.2: Measured and expected beam contaminations.

The values of table 4.2 were calculated from the area of the gauss peaks fitted to the data. Since the cross section for Rutherford scattering depends not only on the Z but also on the energy E, it is necessary to integrate the cross section over the thickness of the target (see equation 2.4). Using the relative cross sections α_X (always relative to the cross section of ^{32}Mg) and the relation $I = c \cdot N/\sigma$, where I is the beam intensity, N the number of scattered particles, σ the cross section and c a constant, one gets e.g.

$$\frac{I\,(^{32}\mathrm{Al})}{I\,(^{32}\mathrm{Mg} +^{32}\mathrm{Al} +^{32}\mathrm{Si})} = \frac{\alpha_{Al} N\,(^{32}\mathrm{Al})}{N\,(^{32}\mathrm{Mg}) + \alpha_{Al} N\,(^{32}\mathrm{Al}) + \alpha_{Si} N\,(^{32}\mathrm{Si})}. \quad (4.11)$$

Table 4.2 shows that the different measured beam contaminations and the contamination expected from the β-decay during the trapping and breeding do in all cases agree within the errors, except for the measurement of the $\frac{I(^{32}\mathrm{Si})}{I(^{32}\mathrm{Mg}+^{32}\mathrm{Al}+^{32}\mathrm{Si})}$ with the thin silver target, where a bigger contamination is expected. The relatively large errors for the expected contamination from β-decay stems from the large uncertainties in the lifetime of the concerned isotopes. The conclusion is that the radioactive contamination of the ^{32}Mg beam is only due to the β-decay of ^{32}Mg itself, which is inherent to our technique to produce RIBs. As mentioned before in subsection 3.3.3 it is possible

to distinguish the ^{32}S from the other beam components due to its higher energy loss in the target, which is why it is not considered here.

Chapter 5

Setup and Efficiency for d(^{30}Mg, ^{31}Mg)p

5.1 Setup

The setup of the transfer experiment d(^{30}Mg, ^{31}Mg)p is the same as the one described in section 3.1, except that the two ΔE detectors were not yet installed in 2003. In particular the CD detector is used to detect the energy and the angle of protons from the reaction and elastic scattered particles. The target used was a 10 μm ($\approx$ 0.92 mg/cm^2) thick foil of deuterated polyethylene (PE) and the beam energy was 2.25 MeV/u. All γ-spectra were recorded in coincidence with a particle detected in the CD detector.

5.2 Efficiency

The efficiency of the whole MINIBALL setup was measured with a ^{152}Eu source (see figure 5.1). In order to determine the relative efficiency the intensities of the different lines were measured, normalized to one transition and compared to the known intensities of the source.

In order to obtain an absolute calibration point the coincidence method was used. If a gate is applied to a transition with an energy E_1 that populates a state that further decays by a transition of energy E_2, then for each detected γ-ray with energy E_1 one γ-ray of energy E_2 is emitted. Thus the number of detected γ-rays of energy E_1 $n(E_1)$ and the number of detected γ-rays of energy E_2 in coincidence with a γ-ray of energy E_1 $n_{E_1}(E_2)$ yields the total efficiency $\varepsilon_{tot}(E_2)$

$$\varepsilon_{tot}(E_2) = \frac{n_{E_1}(E_2)}{n(E_1)}. \tag{5.1}$$

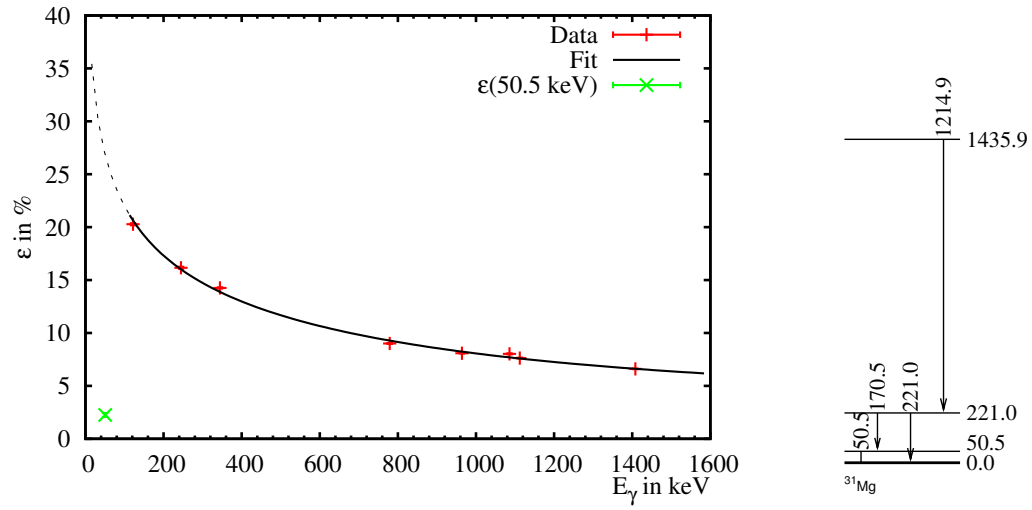

Figure 5.1: Absolute efficiency as measured with a ^{152}Eu source with fit (left panel) with efficiency for the 51 keV line of ^{31}Mg. Schematic level scheme of ^{31}Mg (right panel).

The results of these measurement were fitted, resulting in an efficiency function

$$\varepsilon(E) = \frac{175.863}{E^{0.0511956}} + 0.00169867 \cdot E - 117.11.$$

This function was used to calculate the efficiencies for all energies in the range of 122 to 1408 keV (range of lines from the ^{152}Eu source).

Since the lowest line of this source is at 122 keV it is not possible to deduce the efficiency of MINIBALL for the 51 keV line emitted in the decay of the first excited state of ^{31}Mg (see figure 5.1, right panel). Additionally due to the long lifetime of the 51 keV state the assumption that ^{31}Mg decays at the target position is likely to be wrong which leads to a smaller detection efficiency. On the other hand is the efficiency suppression due to the long lifetime always the same, so the know level structure of ^{31}Mg can be used to extract the efficiency of MINIBALL to detect the 51 keV γ-rays emitted by the de-excitation of the first excited state of ^{31}Mg.

This can be done e.g. by comparing the 51 keV line with the 171 keV line. Those two lines form a cascade that de-excites the 221 keV level. So if a direct feeding of the 51 keV level can be excluded the ratio of the areas of the two peaks is equal to the ratio of the efficiencies of MINIBALL at the two energies.

One way to exclude a feeding of the 51 keV level is by using the γ-γ coincidence spectrum and by gating on the 171 keV line (see figure 7.1). If

$n(E)$ is the number of detected γ-rays of energy E and $\varepsilon(E)$ the efficiency of MINIBALL at energy E, then the number of detected coincident γ-rays $n_{171}(51\text{ keV})$ is

$$\begin{aligned} n_{171}(51\text{ keV}) &= n(171\text{ keV}) \cdot \varepsilon(51\text{ keV}) \\ \Rightarrow\ \varepsilon(51\text{ keV}) &= \frac{n_{171}(51\text{ keV})}{n(171\text{ keV})} \end{aligned} \tag{5.2}$$

where $n(171\text{ keV})$ is the number of detected γ-rays with energy 171 keV,

The same results can be obtained by using a gate on the 51 keV line and observing the 171 keV peak. These two methods yield the same result $\varepsilon(51\text{ keV}) = 2.33(27)$ % (gate on 51 keV) and $\varepsilon(51\text{ keV}) = 2.13(25)$ % (gate on 171 keV).

An other way to exclude the feeding is by taking a look at the spectrum of γ-rays coincident to γ-rays from the 1215 keV line (see figure 7.2). This transition populates the 221 keV level, which decays via a cascade of 171 keV and 51 keV transitions, the ratio of the numbers of detected γ-rays for the 171 and 51 keV lines reflects the ratio between the efficiencies of MINIBALL at the respective energies:

$$\begin{aligned} \varepsilon(51\text{ keV}) &= \varepsilon(171\text{ keV}) \cdot \frac{n_{1215}(51\text{ keV})}{n_{1215}(171\text{ keV})} \\ &= 3.4(11)\ \% \end{aligned} \tag{5.3}$$

with $\varepsilon(E)$ = efficiency of MINIBALL at energy E, $n_{1215}(E)$ = number of detected γ-rays of energy E in coincidence with the 1215 keV γ transition.

These results all agree within their errors and an weighted average of the values gives an efficiency of

$$\varepsilon(51\text{ keV}) = 2.25(18)\ \%.$$

This efficiency will be used in all further calculations.

Chapter 6

Analysis

6.1 Kinematics

The setup (see chapter 5) of the MINIBALL experiment only allows to measure particles with a laboratory scattering angle ϑ_{lab} between about 15° and 55°. For the measurement of the products of the reaction d(^{30}Mg, ^{31}Mg)p that means that it is not possible to directly detect the ^{31}Mg since the maximum angle of ^{31}Mg is less than 3°.

The conservation of momentum and energy in the two-body scattering determines the observed laboratory energy in dependence of the laboratory scattering angle.

Figure 6.1 shows this correlation for the d(^{30}Mg, ^{31}Mg)p reaction under the assumption that it takes place in the middle of the target. That means that the energy of ^{30}Mg was corrected for the energy loss in the first half of the target and the energies of the protons were corrected for the energy loss in the second half of the target considering the different angles of the protons.

Within the angular range covered by the CD detector protons from events with excitation energies up to 2 MeV and scattering angles in the cm system between 100° and 140° are detected.

6.2 Particle Detector

In figure 6.2 (left panel) the measured laboratory energy E versus the laboratory angle ϑ_{lab} is plotted. As discussed in section 6.1 the particles that are directly detected are ^{1}H, ^{2}H, ^{3}H, ^{12}C and ^{30}Mg. The spectrum is dominated by particles from elastic (Rutherford) scattering due to the higher cross section.

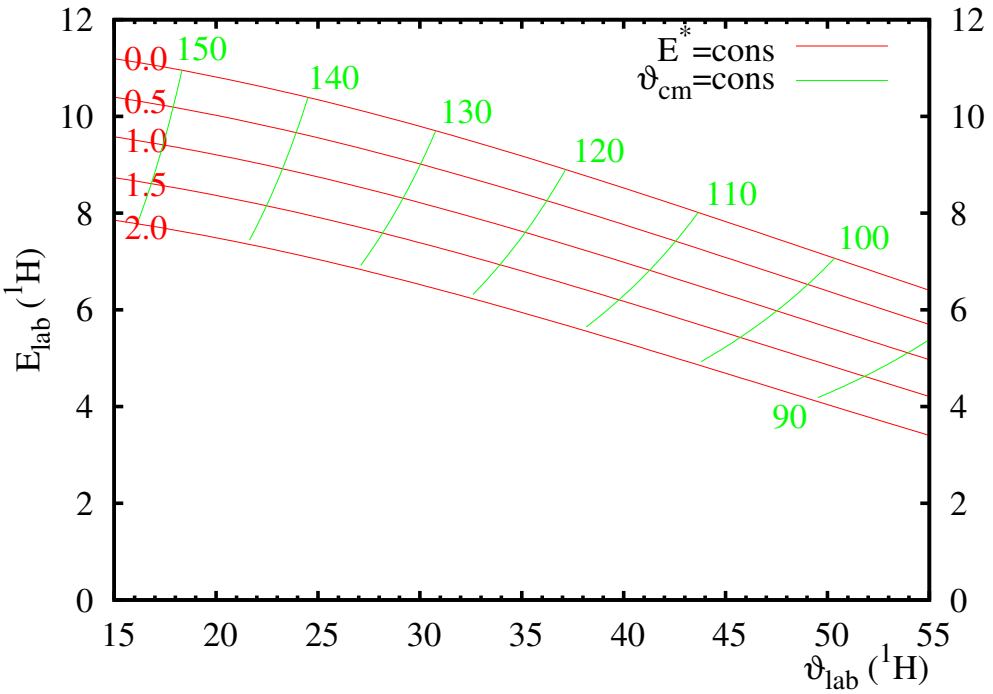

Figure 6.1: Laboratory energy versus laboratory angle for protons from the d(^{30}Mg, ^{31}Mg)p reaction. Different excitation energies from 0 to 2 MeV (red curves) are plotted together with the corresponding scattering angle of the ^{31}Mg in the cm-system (green curves).

The particles with the highest energies are from the elastic scattering of ^{30}Mg on the ^{12}C of the PE target and are thus easily distinguished from the hydrogen isotopes. The two other main contributions are elastic scattered deuterons and protons.

The protons from the (d,p) reaction which are the particles of interest have a slightly different kinematic than the protons from elastic scattering and, if the ground state of ^{31}Mg is populated, show a similar behavior as the elastically scattered deuterons. If higher lying states of ^{31}Mg are populated the energy of the protons is accordingly lower.

Additionally there are also tritons detected from the d(^{30}Mg, ^{29}Mg)t reaction, which are also in the same energy and angle region as the other hydrogen isotopes.

The black lines shown in the plot are the calculated relations of energy and laboratory scattering angle for elastic scattering of ^{1}H, ^{2}H, ^{12}C and ^{30}Mg and the red lines are the same for protons from the (d, p) reaction if the

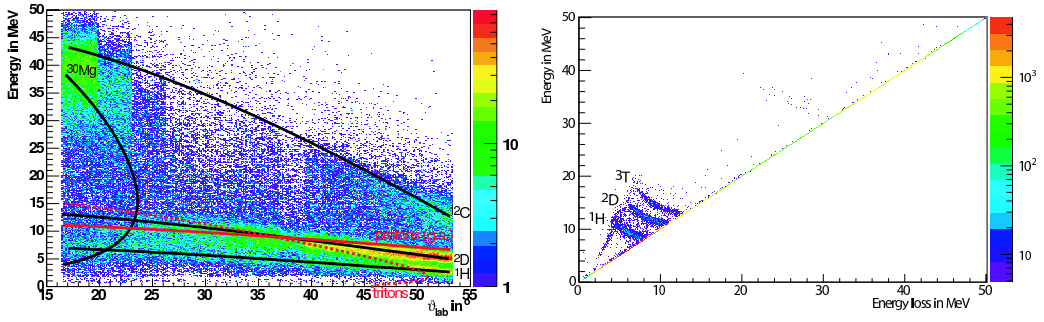

Figure 6.2: Laboratory energy of particles vs. laboratory angle on the left and energy loss in CD on the right without any cuts applied. The black lines are the calculated energies of elastic scattered particles while the red line corresponds to the calculation for the protons and tritons from the transfer reactions.

ground state of ^{31}Mg is populated (solid) and tritons from the (d, t) reaction if the ground state of ^{29}Mg is populated (dashed).

Comparison of the amount of elastic scattered deuterons and protons yields about 10% protons in the target, which is an higher amount than measured in other experiments with the same target material ($\approx$ 4%). This might point toward external contamination of the target with proton containing materials such as vacuum oil.

The right spectrum of figure 6.2 shows the sum of the energies detected in the CD and the CDE detector versus the energy detected in the CD detector[1].

The diagonal represents all the particles that were stopped in the CD detector so that the total detected energy is equal to the energy detected in the CD detector. The three branches that branch off of the diagonal to the top left are particles that lose some energy in the CD detector and are stopped in the CDE detector. There are also particles that are not stopped in the two CD detectors which show up at the end of the three branches almost parallel to the diagonal.

A comparison of the two spectra of 6.2 shows that unfortunately the E vs. ΔE doesn't help to distinguish the protons of interest from the deuterons and tritons, since protons with an energy of less than 8 MeV are stopped in the CD detector and most protons from the (d, p) reaction are below that energy. This means that cuts on lines from the γ spectrum are the only way to distinguish the different reaction channels.

[1]Normally this would be a ΔE vs. E plot, but this way it is easier to compare the left

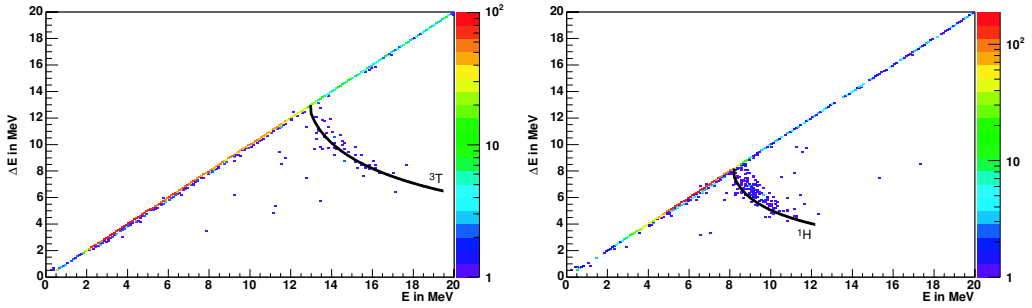

Figure 6.3: ΔE vs. E plots with cuts on γ lines from ^{29}Mg (left) and ^{31}Mg (right). The lines are the calculated energy losses for the smallest laboratory scattering angle that can be detected with the CD detector.

The three branches that branch of the diagonal in the right plot are particles of the three types of hydrogen isotopes that are not stopped in the first CD detector. The lowest branch corresponds to the protons, the second to the deuterons and the highest branch to the tritons. This was also confirmed by only plotting particles for which a coincident γ with an energy of 54 keV (from ^{29}Mg) and 171 keV (from ^{31}Mg) was detected, respectively. With a gate on the γ-line of ^{29}Mg only the highest branch (tritons from the (d,t) reaction) appears and with a gate on the γ-line of ^{31}Mg only the lowest branch appears (protons from the (d,p) reaction), as seen in figure 6.3.

In order to reduce the background there are two possibilities for a cut on the ΔE vs. E spectrum, either on the lowest branch only, which ensures that only protons are selected or on said branch and on the diagonal up to the lowest branch which gives higher statistics but would also select deuterons and tritons with low energies, thus increasing the background. But as said before, the protons that have a high enough energy to penetrate the CD detector are mostly those that are not of interest since they correspond to a population of the ground state of ^{31}Mg, which is why the applied cut is $2 \cdot E_{\mathrm{CD}} + E_{\mathrm{CDE}} < 17\mathrm{MeV}$, which rejects all particles other than protons with an energy in excess of 8.5 MeV.

6.2.1 Particle Reconstruction

Since ^{31}Mg can not be directly detected, its momentum and energy are reconstructed under the assumption that the detected particle is a proton and that the reaction took place in the middle of the target. In order to do this first

spectrum with the right spectrum

the energy and the momentum of the proton in the middle of the target is reconstructed from the data of the CD and the CDE detector and then transformed into the center of mass system. In the cm-system the conservation of momentum gives

$$p_{^{31}\mathrm{Mg}} = -p_{^{1}\mathrm{H}}. \tag{6.1}$$

From the conservation of energy follows

$$E_{^{31}\mathrm{Mg}} = E_{cm} + Q - E_{^{1}\mathrm{H}}. \tag{6.2}$$

With the known momentum and energy four-vector of the reconstructed particle in the cm-system the four-vectors of the reconstructed particle in the laboratory system with and without the energy loss in the target can be calculated.

The excitation energy of the ^{31}Mg can be calculated with the formula

$$E_{ex} = m_0^* - m_0(g.s.) = \sqrt{E^2 - p^2} - m_0(g.s.)$$

where m_0^* is the rest mass of the excited particle, $m_0(g.s.)$ is the rest mass of the particle in its ground state and E and p are the total relativistic energy and momentum of the particle, respectively.

Figure 6.4 shows the Doppler corrected γ energy versus the reconstructed excitation energy of ^{31}Mg. Several strong γ lines are visible at low energies (50.5, 170.5 and 221 keV from ^{31}Mg) as well as other ^{31}Mg lines and a line at 1214.7 keV, indicated by horizontal arrows. The solid line shown in the plot is a cut which represents the fact that the excitation energy has to be larger or equal to the energy of a γ transition.

Cuts on the two γ lines at 171 and 1215 keV and projection on the E_{ex} axis yield spectra of the excitation energy as seen in figure 6.5. This plot shows that the 221 keV level, which is depopulated by the 171 keV line, is fed from a higher state through the 1215 keV transition. The counts of the 1215 keV line are corrected by a factor $\varepsilon(171\mathrm{keV})/\varepsilon(1215\mathrm{keV})$, to account for the different γ efficiencies of the two lines.

Figure 6.6 shows the measured γ spectrum with a coincidence condition between the γ-rays and a particle, a cut on the protons (the proton branch from figure 6.2 as well as the diagonal up to said branch), a condition on the reconstructed excitation energy of ^{31}Mg and with random background subtracted. The condition on the excitation energy is

$$E_{ex} > E_{\gamma} - 0.635 \text{ MeV}$$

which removes background from events corresponding to excitation energies below the energy of the γ (minus a value due to a shift of the centroid and the resolution).

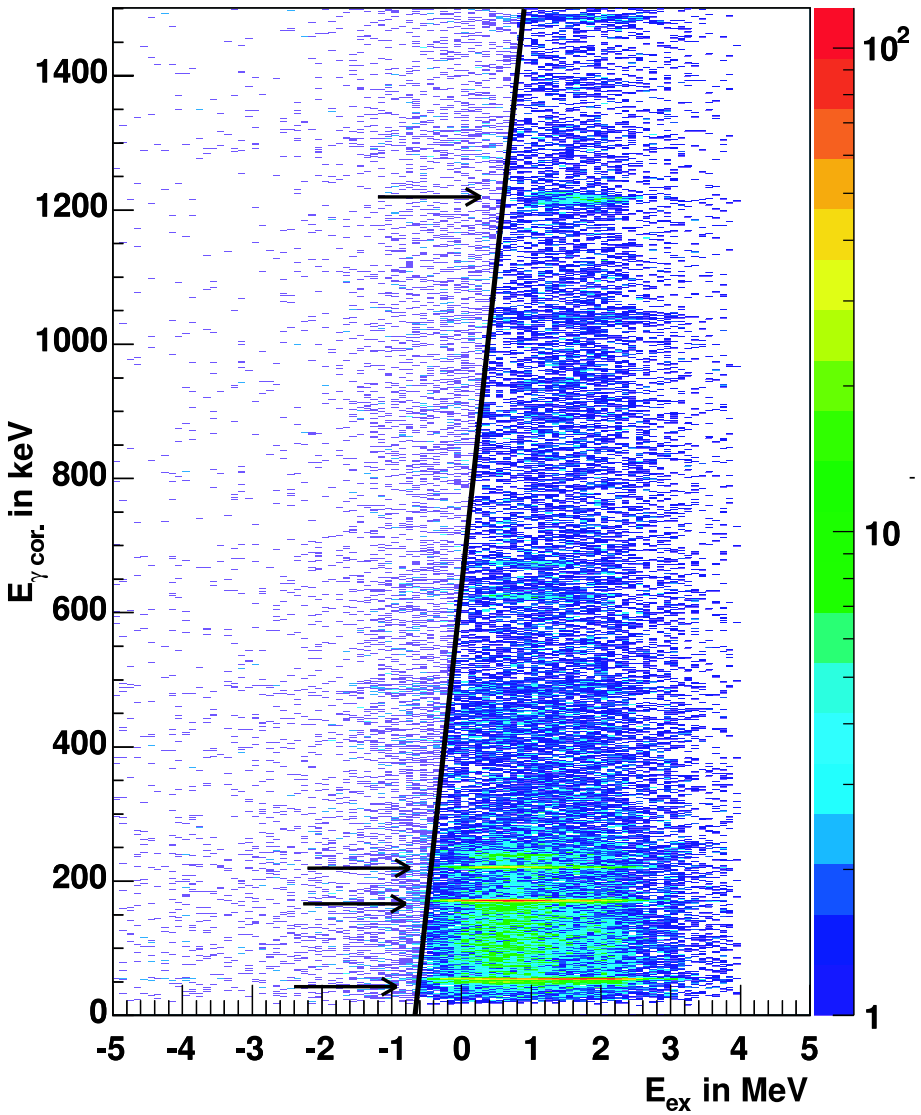

Figure 6.4: Doppler corrected γ energy versus excitation energy. Applied cuts are for coincident γ-rays and particles either in the proton branch of the ΔE vs. E plot (figure 6.2) or on the diagonal below the branch.

After the background subtraction two lines from ^{30}Al are still visible in the spectrum. Since the Doppler correction only works for particles close to the target it is improbable that the lines stem from in-flight β-decay of ^{30}Mg but it is rather probable that the γ-rays come from (Coulomb) excitation of ^{30}Al in the beam (about 18 %, see table 4.1.2, page 35).

In the spectrum of figure 6.6 one can see the lines from the ^{31}Mg as well as lines from ^{29}Mg (from (d,t) reaction), ^{30}Mg (inelastic excitation by ^{12}C

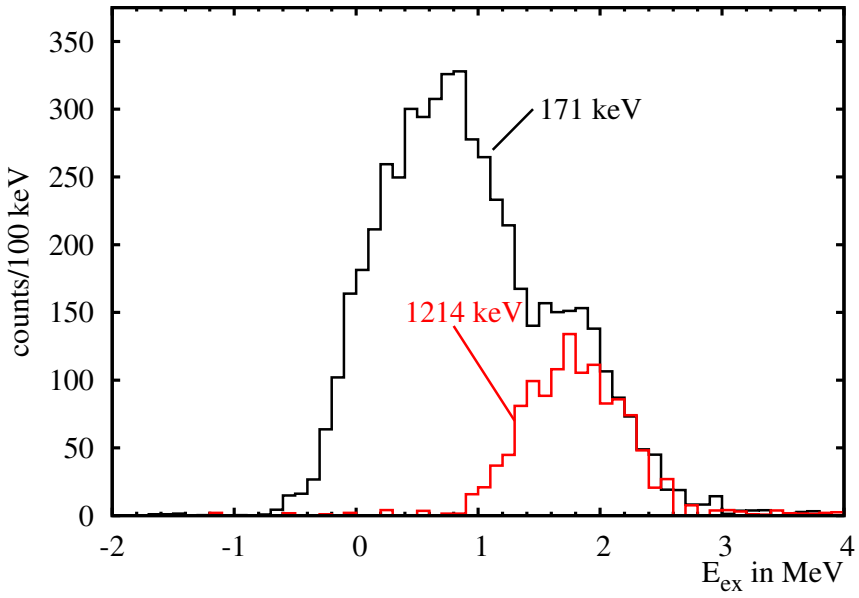

Figure 6.5: Spectrum of excitation energy for the 171 keV and the 1215 keV line of ^{31}Mg after background subtraction. The counts in the 1215 keV line were corrected by a factor $\varepsilon(171\text{keV})/\varepsilon(1215\text{keV})$, to account for the different γ efficiencies of MINIBALL for the two lines.

and ^{2}D) and ^{30}Al (see above).

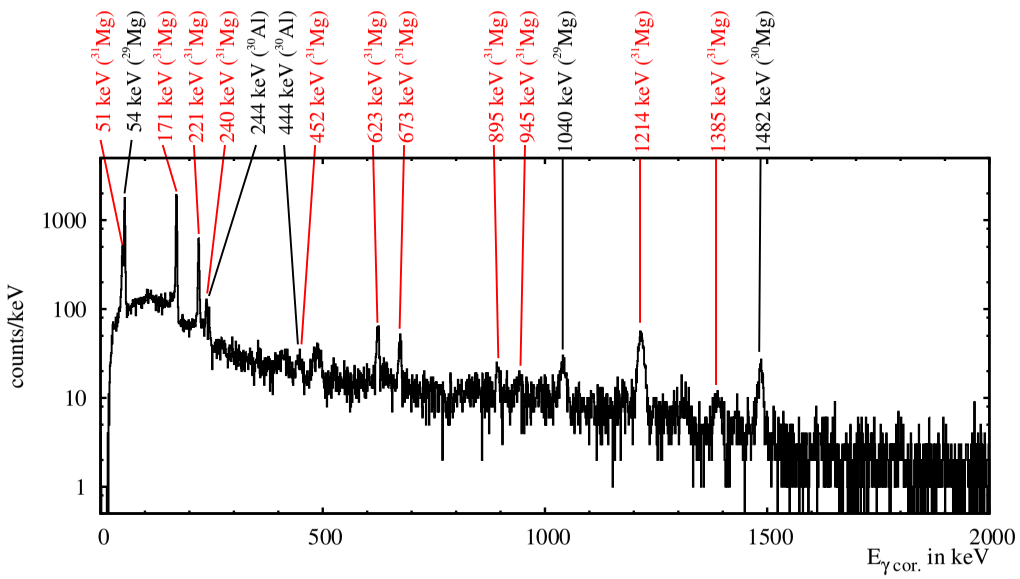

Figure 6.6: Doppler corrected coincident γ spectrum with a cut on protons and E_{ex} and $E_{\gamma cor.}$ as shown by the line in figure 6.4.

Chapter 7

Results

E_γ *lit.*	E_γ *fit*	N_γ	$N_\gamma/\varepsilon_\gamma$	Nucleus	Reaction
50.5(7)	48.97(28)	1291(100)	58170(5208)	^{31}Mg	(d,p)
54.6(1)	53.74(26)	4222(165)	16035(626)	^{29}Mg	(d,t)
170.5(8)	170.24(34)	5411(269)	29452(1464)	^{31}Mg	(d,p)
221.0(4)	219.92(39)	1634(88)	9805(530)	^{31}Mg	(d,p)
240.0(10)	237.37(45)	274(36)	1696(225)	^{31}Mg	(d,p)
243.89(8)	243.18(55)	130(29)	812(181)	^{30}Al	(d,d), (C,C)
443.62(15)	442.72(67)	36(12)	293(100)	^{30}Al	(d,d), (C,C)
452.1(13)	450.83(98)	28(12)	231(94)	^{31}Mg	(d,p)
622.6(14)	622.03(90)	279(23)	2674(223)	^{31}Mg	(d,p)
673.1(12)	671.79(99)	177(19)	1761(193)	^{31}Mg	(d,p)
894.6(11)	890.56(141)	75(16)	870(187)	^{31}Mg	(d,p)
945.1(10)	941.30(162)	51(15)	608(175)	^{31}Mg	(d,p)
1040.0(10)	1037.71(158)	175(22)	2223(276)	^{29}Mg	(d,t)
1214.9(9)	1212.70(167)	662(31)	9185(432)	^{31}Mg	(d,p)
1385.4(12)	1384.14(222)	103(18)	1538(270)	^{31}Mg	(d,p)
1482.1(5)	1481.15(207)	205(19)	3192(295)	^{30}Mg	(d,d), (C,C)

Table 7.1: Direct and efficiency corrected results of integration of all lines.

From the integration of the peaks in the spectrum from figure 6.6 the number of detected γ-rays for each line of the ^{31}Mg was determined. These numbers were corrected with the efficiency of the MINIBALL setup and are presented in table 7.1.

The line at 240 keV poses a problem since it is close to the 243.89(8) keV line of ^{30}Al. Additionally the corresponding level at 461 keV has a long lifetime (10.5(8)ns [16]), which means that the assumption that the excited

^{31}Mg decays in the target is wrong which in turn leads to smaller detection efficiencies.

The line at 452.1 keV is also problematic since it overlaps with the other ^{30}Al line at 443.62(15) keV. Because of the lifetime of the 461 keV state it is only possible to give a lower limit for the 240 keV line and the line at 452.1 keV is so small that it is only acceptable as a line because it is exactly at the expected energy for a transition from the 673.1 keV state to the 221.0 keV state (the statistic is too small to see it γ-γ coincidences).

7.1 Level Scheme

Figure 7.3 shows the level scheme of ^{31}Mg as it was measured in this experiment. The black levels and transitions were already previously recorded [17], the red level at 1435.9 keV is a new proposition based on the new placement of the 1215 keV transition.

The branching ratio given above the transition in figure 7.3 and in table 7.2 result from assigning the strongest line of the level an intensity of 100 and calculating the relative intensities of the other lines correspondingly.

The number of detected γ-rays (efficiency corrected) are given in small script at the arrows of each transition. Assigning the 50.5 keV line an intensity of 100, the relative intensities of the lines that belong to the same level were calculated.

Subtracting the number of produced γ-rays that feed a state from the number of produced γ-rays that empty the same state provides how often that state was directly populated by the (d, p) reaction. These numbers are given on the left side of each state.

The proposition of the new level at 1435.9 keV is based on the spectrum of coincident γ-rays for the 171 keV and the 1215 keV line. Figure 7.1 shows the spectrum of γ-rays that are coincident with a proton and an other γ from the 171 keV line. The spectrum shows a clear coincidence between the 171 keV line and the 51 keV line, the 240 keV line and the 1215 keV line. The corresponding spectrum of γ-rays coincident with the 1215 keV line is shown in figure 7.2. This spectrum also shows a strong coincidence between the 1215 keV and the 171 keV line, as well as the 51 keV line and the 221 keV line which all belong to the de-excitation of the 221 keV level. On the other hand there is no sign that the 1215 keV line populates a level at 1029 keV, which would decay to the 221 keV level via 808 keV transition as it should according to [17, 18].

The newly observed γ transition with 1385 keV provides additional evidence for the new level at 1435.9 keV. A coincidence with the 51 keV line

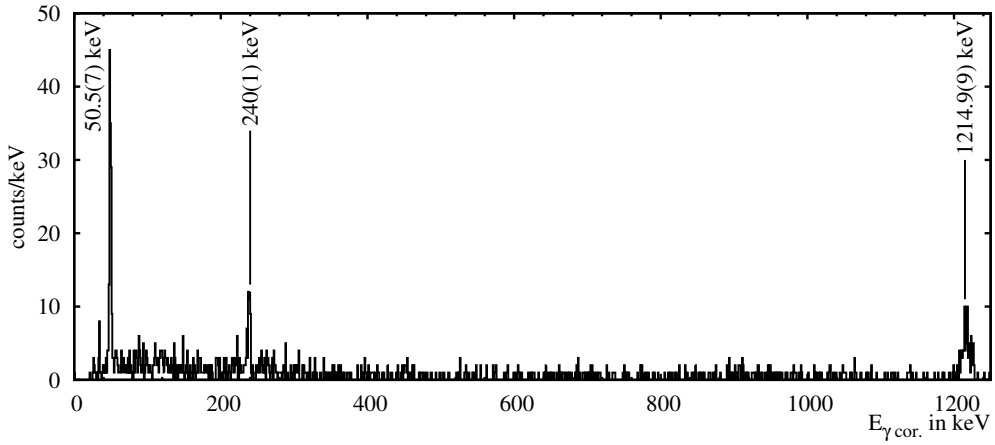

Figure 7.1: Coincident γ spectrum for a γ energy of $167 - 174$ keV.

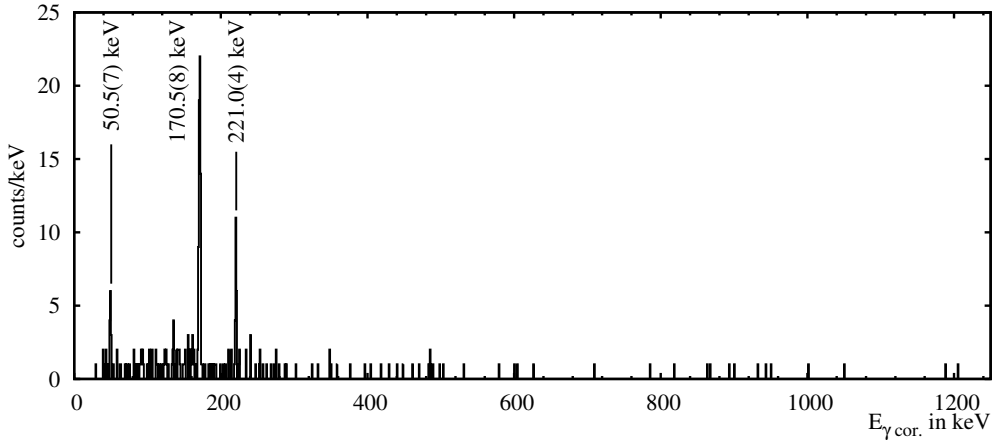

Figure 7.2: Coincident γ spectrum for a γ energy of $1210 - 1223$ keV.

could not be observed due to the low intensity of the line and the long lifetime of the 51 keV level. But the energy difference between this line and the 1215 keV line matches the energy difference between the 51 keV and the 221 keV levels, providing additional support that the 1215 keV line decays from a state at 1436 keV to the 221 keV level.

Another newly observed transition is from the 945.1 keV level into the ground state. This is a further confirmation of the 945.1 keV level which was proposed in [17] from the coincidence of the 894.6 keV line with the 51 keV line. This coincidence could not be measured in this experiment due to the

low statistics (only 75(16) counts in the 894.6 keV line).

E_i *in keV*	E_γ *in keV*	E_f *in keV*	*relative* γ *branching ratio*	*Lit.*
50.5	0	50.5	100	100
221	0	221	35.0(22)	40.8(30)
221	50.5	170.5	100	100
461	221	240	100	100
673.1	0	673.1	63.7(91)	43.8(37)
673.1	50.5	622.6	100	100
(673.1	221	452.1	11.0(52)	12.5(32))
945.1	0	945.1	70.(25)	0
945.1	50.5	894.6	100	100
1435.7	50.5	1385.4	16.7(30)	0
1435.7	221	1214.9	100	100

Table 7.2: Branching ratios of ^{31}Mg transitions.

The determined branching ratios of this study (see table 7.2) differ somewhat from the results of [17]. The value for the 452.1 keV line is given in brackets because of the earlier mentioned problems with an overlap with the 443.62 keV line of ^{30}Al. The branching ratios were determined directly from the efficiency corrected areas of the peaks (see table 7.1).

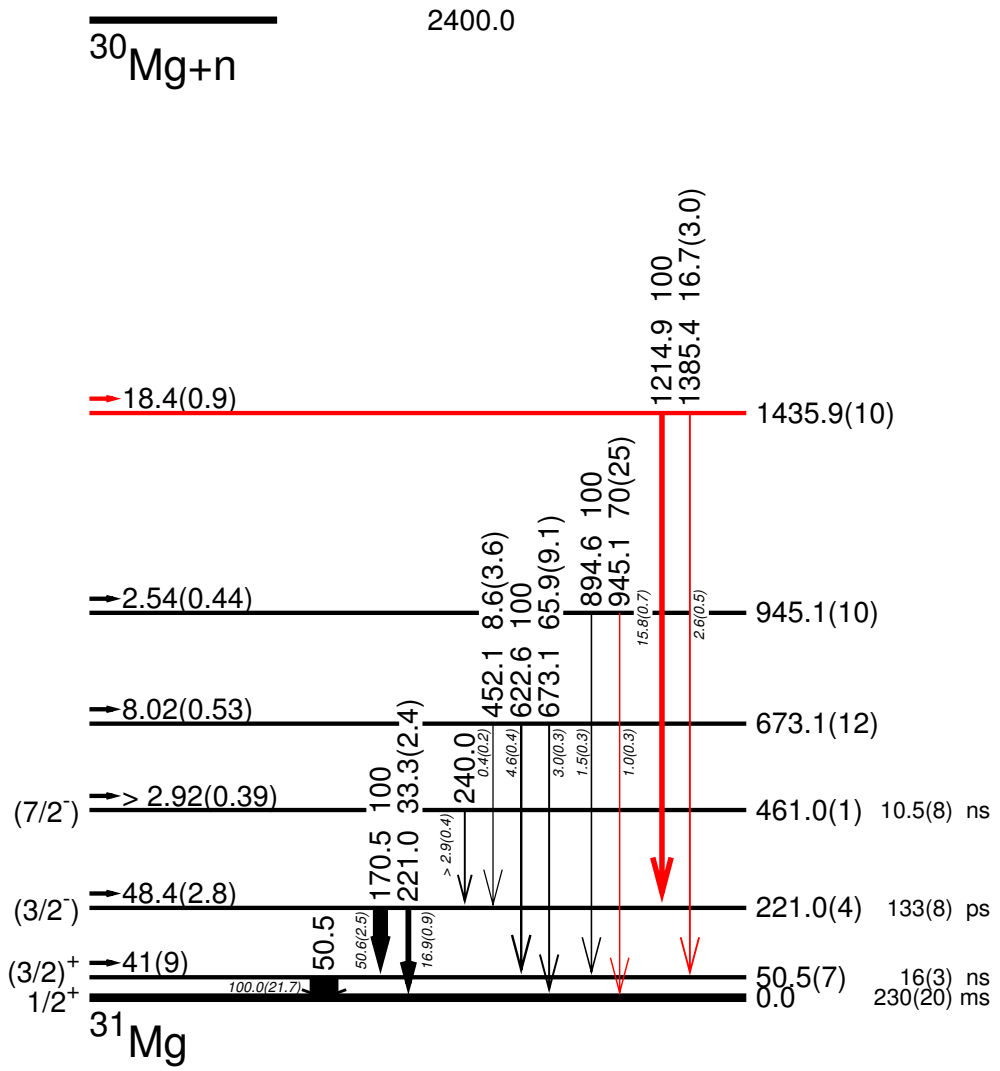

Figure 7.3: Level scheme of ^{31}Mg as seen in the d(^{30}Mg, ^{31}Mg)p reaction at 2.25 MeV/u: the small numbers next to the transition arrows are the efficiency corrected intensities of the γ lines, while the numbers above the levels on the left are the relative cross section for populating the level, determined from the ε-corrected line intensities. The level spins are from [19] and the lifetimes from [16, 17].

Chapter 8

Conclusion and Outlook

In the first part of this thesis the results of the installation of two ΔE detectors were presented. It was possible to qualitatively and quantitatively measure the beam contamination at REX-ISOLDE which is important for experiments like the $B(E2;\ 0^+_{\mathrm{gs}} \rightarrow 2^+_1)$ measurement of ^{32}Mg. Various sources of beam contamination were identified

- coming directly from the ISOLDE target,
- originating from β-decay during trapping and breeding and
- stable contamination from residual gas of the EBIS

and studied not only with the installed ΔE detectors but also by

- the analysis of the release curve,
- the measurement of β-decay in the beam dump and
- a RILIS on/off measurement.

It was shown that the results of the different methods do agree and that the beam contamination is stable over the time of an experiment.

In the second part a study of ^{31}Mg via the ^{30}Mg (d, p) ^{31}Mg reaction was performed. This study has proven helpful in furthering the knowledge about the excited states of ^{31}Mg.

A wrong placement of the 1215 keV γ line has been corrected, introducing a new state with an excitation energy of 1436.7 keV. This state has been confirmed by the observation of another transition from this state to the first excited state at 51 keV with an energy of 1385 keV.

Furthermore, the state with excitation energy of 945 keV was confirmed by observing a transition directly to the ground state in addition to the known transition of 895 keV to the first excited state.

Further information about the spin of the states (so far only the spin of the ground state is definitely known as $1/2^+$ [19]) may be obtained by studying the angular distributions of the protons and comparing them to theory.

In order to do so it will be necessary to calculate the cross section $\mathrm{d}\sigma/\mathrm{d}\Omega(\vartheta)$ for the protons which means it will be necessary to determine the amount of particles in the beam. This can be done by comparing the amount of elastic scattered particles with the results of a Monte Carlo simulation. For the angular distribution of protons for the 221 keV state corrections for the feeding by the 1215 keV state have to be made.

Acknowledgments

Special thanks go to Prof. Dr. Dirk Schwalm and Dr. Heiko Scheit for their support and help throughout the work on this thesis. Their doors were always open and they've given invaluable input for the thesis.

I want to thank all the members of the CB group for their support, namely Hans Boie, Dr. Frank Koeck and Dr. Martin Lauer. A special thanks goes to Oliver Niedermaier who supplied me with the code for the analysis and helped me understanding it.

I want to thank Dr. Gerhard Schrieder for providing the ΔE detectors and supporting my thesis.

I want to thank the MINIBALL collaboration for the setup and support of the experiments. Without all the previous hard work that went into getting MINIBALL operational this thesis hadn't been possible.

I want to thank the ISOLDE workers for their hard work to providing us with beam and especially Dr. Thomas Sieber from REX.

Finally I want to thank my family and my friends for their support and for taking my mind off physics.

Bibliography

[1] D. Habs, O. Kester, T. Sieber, H. Bongers, S. Emhofer, P. Reiter, P. Thirolf, G. Bollen, J. Äystö, O. Forstner, et al., Hyperf. Int. **129**, 43 (2000).

[2] O. Kester, T. Sieber, S. Emhofer, F. Ames, K. Reisinger, P. Reiter, P. Thirolf, R. Lutter, D. Habs, B. Wolf, et al., Nucl. Instr. Meth. B **204**, 20 (2003).

[3] O. Niedermaier, H. Scheit, V. Bildstein, H. Boie, J. Fitting, R. von Hahn, F. Köck, M. Lauer, U. Pal, H. Podlech, et al., Phys. Rev. Lett. **94**, 172501 (2005).

[4] J. Eberth, G. Pascovici, H. Thomas, N. Warr, D. Weisshaar, D. Habs, P. Reiter, P. Thirolf, D. Schwalm, C. Gund, et al., Prog. Part. Nucl. Phys. **46**, 389 (2001).

[5] E. K. Warburton, J. A. Becker, and B. A. Brown, Phys. Rev. C **41**, 1147 (1990).

[6] O. T. Niedermaier, Dissertation, Universität Heidelberg (2005).

[7] G. R. Satchler, *Introduction to Nuclear Reactions* (Oxford University Press, 1990).

[8] J. Lindhard, M. Scharff, and H. E. Schiøtt, Mat. Fys. Medd. Dan. Vid. Selsk. **33**, No. 14 (1963).

[9] H. Ernst and K. Lesko, *Irma code* (1984).

[10] J. F. Ziegler, *Handbook of Stopping Cross-Sections for Energetic Ions in all Elements* (Pergamon Press, 1980), vol. 5 of *The Stopping and Ranges of Ions in Matter*, chap. 2, p. 12 et sqq.

[11] J. F. Ziegler, J. P. Biersack, and U. Littmark, *The Stopping and Range of Ions in Solids* (Pergamon Press, 1985), vol. 1 of *The Stopping and Ranges of Ions in Matter*, chap. 2, p. 50 et sqq.

[12] J. Cederkäll, F. Ames, P. Butler, P. Delahaye, V. Fedoseev, M. Lindroos, T. Nilsson, T. Sieber, F. Wenander, M. Pantea, et al., Nucl. Phys. A **746**, 17 (2004).

[13] A. Ostrowski, S. Cherubini, T. Davinson, D. Groombridge, A. Laird, A. Musumarra, A. Ninane, A. di Pietro, A. Shotter, and P. Woods, Nucl. Instr. Meth. A **480**, 448 (2002).

[14] J. Lettry, R. Catherall, P. Drumm, P. Van Duppen, A. H. M. Evensen, G. J. Focker, A. Jockinen, O. C. Jonsson, E. Kugler, H. Ravn, et al., Nucl. Instr. Meth. B **126**, 130 (1997).

[15] U. Köster, V. N. Fedoseyev, A. N. Andreyev, U. C. Bergmann, R. Catherall, J. Cederkäll, M. Dietrich, H. De Witte, D. V. Fedorov, L. Fraile, et al., Nucl. Instr. Meth. B **204**, 347 (2003).

[16] H. M. et al., *Ultra fast time-delayed studies on ^{30}Mg, ^{31}Mg and ^{32}Mg*, Poster on INPC, Gøteborg (2004).

[17] G. Klotz, P. Baumann, M. Bounajma, A. Huck, A. Knipper, G. Walter, G. Marguier, C. Richard-Serre, A. Poves, and J. Retamosa, Phys. Rev. C **47**, 2502 (1993).

[18] D. Guillemaud-Mueller, C. Détraz, M. Langevin, F. Naulin, M. de Saint-Simon, C. Thibault, F. Touchard, and M. Epherre, Nucl. Phys. A **426**, 37 (1984).

[19] G. Neyens, M. Kowalska, D. Yordanov, K. Blaum, P. Himpe, P. Lievens, S. Mallion, R. Neugart, N. Vermeulen, Y. Utsuno, et al., Phys. Rev. Lett. **94**, 022501 (2005).

Erklärung:

Ich versichere, daß ich diese Arbeit selbständig verfaßt und keine anderen als die angegebenen Quellen und Hilfsmittel benutzt habe.

Heidelberg, den 12.07.2005

.....
(Unterschrift)